REVIEW

Emerging Memristive Artificial Neuron and Synapse Devices for the Neuromorphic Electronics Era

Received 00th January 20xx,
Accepted 00th January 20xx

DOI: 10.1039/x0xx00000x

Jiayi Li,[a] Haider Abbas,[a] Diing Shenp Ang,*[a] Asif Ali,[a] and Xin Ju[b]

Growth of data eases the way to access the world but consumes increasing energy to store and process. Neuromorphic electronics emerged in the last decade, inspired by biological neurons and synapses, with in-memory computing ability, extenuates the 'von Neumann bottleneck' between memory and processor, offers a promising solution to reduce the efforts both in data storage and process thanks to their multi-bit non-volatility, biological-emulated characteristics, and silicon compatibility. This work reviews the recent advances of emerging memristive devices for artificial neuron and synapse applications, including memory and data-processing ability: The physics and characteristics are discussed first, i.e., valance changing, electrochemical metallization, phase changing, interfaced-controlling, charge-trapping, ferroelectric tunnelling, and spin-transfer torquing. Next, we propose a universal benchmark for the artificial synapse devices on spiking energy consumption, standby power consumption, and spike timing. Based on the benchmark, we address the challenges, suggest the guidelines for intra-device and inter-device design, and outlook the neuromorphic applications for the resistive switching-based artificial neuron and synapse devices.

1. Introduction

Ever since the conception of the McCulloch-Pitts neuron [1] and perceptron [2] models in the middle of the 20th century, artificial intelligence (AI) or artificial neural network (ANN) has largely remained a computer science terminology. Progress in the later part of the century was hampered by the lack of computational power. Integrated circuit fabrication in the 1980-2000 period did not allow a high-density integration of transistors on a single processor and memory chip. Therefore, running simulations on deep neural network (DNN) or deep convolutional neural network (DCNN) [3] and storing exponentially accumulating data were impractical in terms of time and energy costs even though ANN models were already relatively well established at that time [4-10]. With increased chip density and the advent of multi-core processors such as the graphic processing unit (GPU) brought by the pursuit of Moore's law, coupled with more efficient ANN algorithms [3, 11, 12], the computational power bottleneck was successfully resolved at the beginning of this century. In 2012, a DNN with a billion connections was shown to be able to recognize highly conceptual objects such as cat and human body [13]. In the same year, the DNN was shown to be on par with the human in terms of image classification accuracy (based on the MNIST database) and it even outperformed the human on traffic sign recognition [14]. Introduced by Maass in 1995[15, 16], spiking neural networks (SNNs) employ spiking neurons, also known as leaky integrate-and-fire (LIF) neurons, to compute. SNN is regarded as the third generation ANN model classified by computational units, where the first generation is marked by MCP Model and the second is characterized with feedforward and recurrent sigmoidal neural nets, such as rectified linear unit (ReLU), as well as networks of radial basis function units [17]. The substantial difference between the second and third generation, as concluded by Roy *et al.* [18], lies in the dynamic of the signal: SNN relies on the temporal dynamics (frequency and interval) of the binary incoming spikes, whereas the former uses the spatial dynamics (amplitude) of the signal.

In recent years, researchers devote lots of focus on implementing SNN computing model on current computational architecture (von Neumann Architecture) and achieve excellent performance on visual and audio processing[19-29]. In this regard, more comprehensive reviews on the emerging software SNN are worth exploring [18, 30]. However, like DNN or CNN, these are typically algorithms implementing different computational cores under conventional von Neumann architecture computing units, which limits the potential of SNN by separating computation, transmission, and storage of the data. As in the brain, which SNN dedicate to mimic, nerve cells and synapses not only transmit the signal electrically (spikes along axons) and chemically (neurotransmitters in synapses), but learn, compute, and memorize as well.

At this juncture, the AI community is confronted with another major challenge – the von Neumann bottleneck. This issue arises from the physically separated processor and memory units in the modern-day computer. While such an architecture could turnaround, in a relatively short time, a general computational job involving low data exchange between the processor and memory, it suffers from considerable time and

[a] School of Electrical and Electronics Engineering, Nanyang Technological University, 50 Nanyang Avenue, Singapore 639798.
[b] Institute of Materials Research and Engineering (IMRE), Agency for Science, Technology and Research (A*STAR), 2 Fusionopolis Way, Singapore 138634.
* Email: edsang@ntu.edu.sg

Please do not adjust margins

energy overheads when executing computationally intensive ANN algorithms. The iterative and recursive nature of such algorithms result in a massive data exchange between the serially interfaced processor and memory, creating therefore a speed bottleneck. While outstanding algorithm optimization work by computer scientists [31, 32] has offered some respite, innovative hardware solutions are now deemed mandatory in view of the imminent data explosion in the current internet-of-things era.

The capability of the human brain in processing massive amounts of data in real time at a minute fraction of the energy cost of the most advanced computers has continued to amaze neuroscientists. In the pursuit of an efficient hardware platform for ANNs, the human brain therefore naturally serves as the golden guide. Attempt to extend existing digital circuit design methodology to mimic the functionality of neurons and synapses in the biological neural network (CMOS-based SNN) has proven futile because of the large footprints and high energy cost of the resultant circuitries [33-35]. Thus, the last few years have seen an intensive amount of research effort being directed at developing alternative building blocks, commonly termed neuromorphic devices, that are both size and energy efficient, dedicated for implementing neuromorphic-device-based SNN, in which scope reviewed by Marković *et al.* who discussed the underlying physics [36], Wang *et al.* who examined the material dependencies [37], and Zhang *et al.* who investigated the chip level implementation [38]. Their works have envisioned a framework of the neuromorphic computing system, where neuromorphic devices will be the foundation.

Therefore, this review paper focuses and summarizes recent major progress in the building block neuromorphic devices. As similarly employed by Demise *et al.*, terms "neuroscience" and "AI" to differentiate the biological/artificial intelligence [30], we carefully use "biological" for discussions in the study of brain, biological neuron and synapses, and their relative behaviours and term "neuromorphic" for discussions in the domain of electronic devices dedicating to emulate the function of brain, biomaterial is not within the scope of this work. Organization of this review is as follows. In section II, we review the basic operation of the biological neural network. Since the exact function of the brain is still a subject of continuing research, only essential concepts that underpin current effort towards a neuromorphic computer are emphasized. Section III details strategies that have been adopted in the current transition phase from von Neumann to a fully neuromorphic architecture. In section IV, we compare various promising neuromorphic memristive candidates for artificial neurons and synapses. These devices are benchmarked according to their action energy and standby power consumption, and spike timing. Section V concludes and presents challenges that remain to be tackled in this major shift in the computing paradigm, highlights potential guidelines on device design, and outlooks the promising neural network level applications.

2. Biological Neural Network

This section describes the building blocks of a biological neural network and their fundamental roles and functions in the cognitive ability of living species. Although how exactly cognition develops is a major question to be answered, some basic principles have closely guided our current efforts in neuromorphic engineering.

A. Basic Function of the Biological Neuron

Unlike in a von Neumann computer where a clear partition exists between the processor and memory, a biological neural network comprises a massive, distributed network of neurons [39], which serve as the basic "computational units". A neuron receives input signals (data), in the form of voltage spikes or action potentials, from neighbouring neurons via synaptic junctions formed between axons of the transmitting (or pre-synaptic) neurons and dendrites of the receiving (or post-synaptic) neuron (Fig. 1a-c). A voltage spike arriving at the axon-end of a synapse triggers an ionic current, comprising sodium ions, that flows into the post-synaptic neuron. This in turn depolarizes the neuron, i.e., causes its membrane potential to increase positively from its negative rest level. As depicted in Fig. 1d, when enough stimulation (V_{IN}) is received by a neuron, its membrane potential rises sharply (V_{MEM}), and this triggers a voltage spike (V_{OUT}) down its axons to other downstream neurons. After the "firing" of a voltage spike, the inflow of sodium current ceases and other channels open to allow an outflux of potassium ions from the neuron. This returns or resets the membrane potential to a negative rest level [40].

In 1943, McCulloch and Pitts captured the accumulative function of the biological neuron that led to the eventual firing of an action potential into a mathematical model known as the McCulloch-Pitts neuron [1], which was the first spiking neuron model ever proposed. In 1952, Hodgkin and Huxley presented a comprehensive analysis of the dynamics of membrane potential under the concerted actuation of multiple ion channels [41]. However, the resultant model, comprising several differential equations, is too complex. Some neuron modelling work, therefore, focused on simplicity, representing the overall function using lumped circuit components, e.g., the integrate-and-fire neuron [42] (Described by a membrane capacitance C), improved leaky integrate-and-fire or LIF neuron [43-45] (Described by a parallel RC circuit). In the LIF neuron model, the shunt resistor R is used to account for the loss of ionic charge from the neuron in-between voltage spikes. Another noteworthy model is the adaptive exponential integrate-and-fire neuron [46-48], capable of describing numerous known firing patterns, e.g., bursting, delayed spike initiation, fast spiking, etc. A comprehensive review on different neuron models can be found in Burkitt *et al.* [49].

B. Basic Function of the Biological Synapse

A von Neumann computer always requires the same amount of time to compute identical or similar data. In contrast, the brain is well known for its ability to learn and can subsequently process similar information in a much shorter time. Although the exact manner by which learning or cognition occurs in the brain remains an open question, this capability has been widely

This journal is © The Royal Society of Chemistry 20xx

Please do not adjust margins

Please do not adjust margins

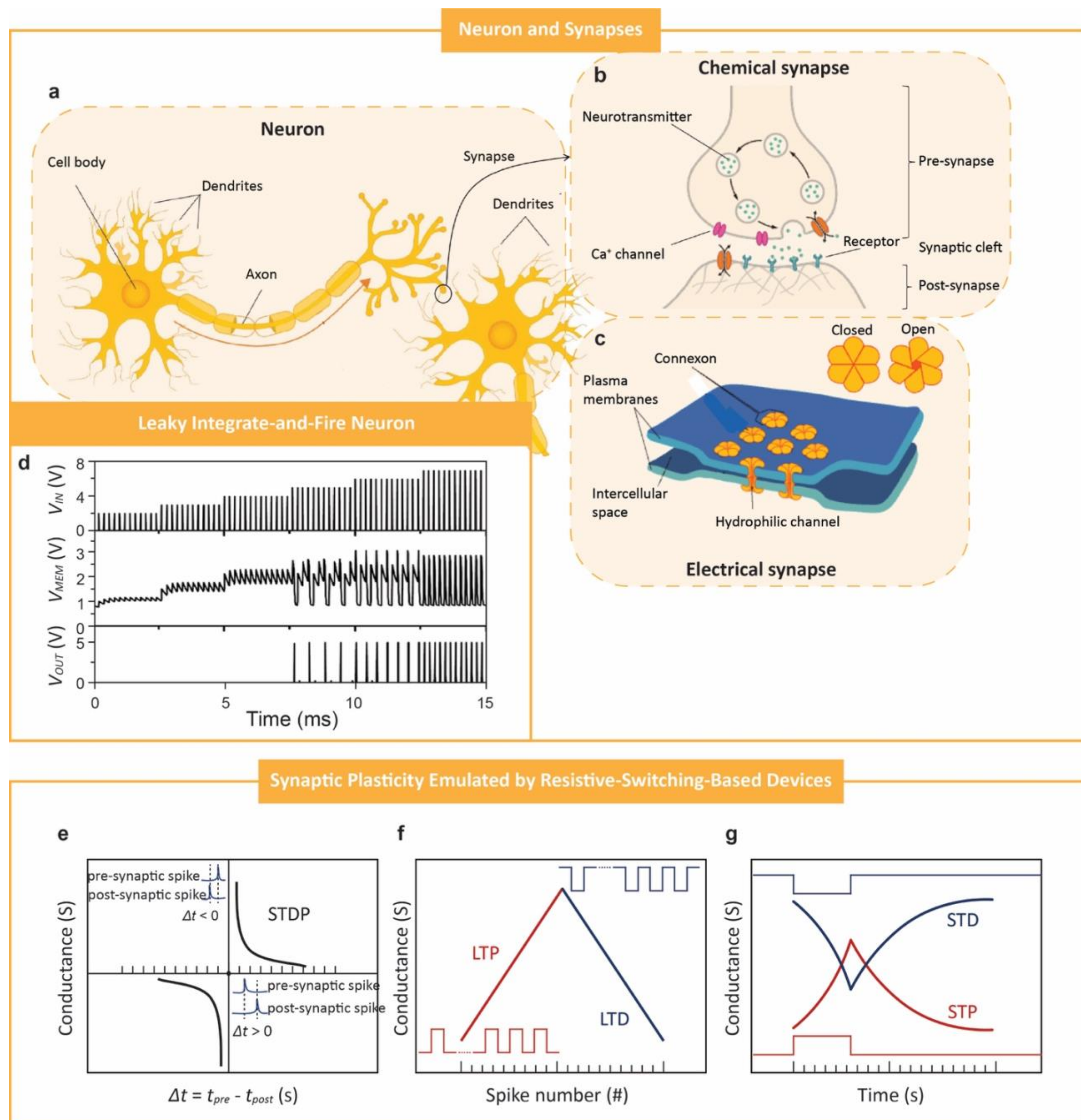

Fig. 1 Building blocks of biological neuron and synapses. a-c, **Neurons and synapses** including the basic structures of common neuron cell (**a**) and the synapses (**b-c**), where the chemical synapse (**b**) and electrical synapse (**c**) are responsible for signal transmission between neurons. **d**, **LIF neuron model.** The neuron could fire a voltage spike after integrating several input voltage spikes and return to rest or off state. The input spikes (V_{IN}) are expected to be larger than the operating threshold of the circuit to start the integration (V_{MEM}) and generate the output (V_{OUT}). **e-g**, **Synaptic functions:** STDP (**e**), LTP and LTD (**f**), STP and STD (**g**). For spiking-time dependent plasticity (STDP) in **e**, the device conductance is modulated by the timing difference of input pre-synaptic spikes and the back propagation of post-synaptic spikes (inset of c), Δt. The larger Δt is, the smaller effect on the device conductance will be, and vice versa. For long term potentiation and depression (LTP and LTD) in **f**, device conductance changes with the consecutive input pulses (insets of **f**) and the initial, final, and intermediate states are stable. For short term potentiation and depression (STP and STD) in **g**, device conductance is modulated by a single or several pulses without permanent change on the conductance. **Credits**: **a-c** are reproduced under a Creative Commons Attribution (CC-BY) license; **d** is reproduced under Creative Commons Attribution (CC-BY) license from ref.[53], copyright Rozenberg *et al.* 2019 Springer Nature.

attributed to the synapses across which neurons communicate [39, 50-52]. During learning, it is believed that synaptic junctions throughout the biological neural network are selectively strengthened or weakened. This process creates a "memory map" comprising a subset of strongly connected neurons responsible for subsequent fast processing and propagation of similar data through the network.

Synapses may be classified into two categories, namely chemical and electrical [40] (Fig. 1b and c). At an electrical synapse, an incoming voltage spike creates a potential difference between the pre- and post-synaptic neurons and

Please do not adjust margins

Please do not adjust margins

directly induces the flow of a sodium ionic current through the pores or intercellular channels that extend across the synaptic cleft [54, 55] (Fig. 1c). An electrical synapse can be either unidirectional or bidirectional and has a high transmission speed since the passive current flow across the gap junction is practically instantaneous. The purpose of electrical synapses is to synchronize the firing of a group of neurons to generate a strong stimulus that in turn triggers a crucial response, e.g., a lifesaving reaction. On the other hand, a chemical synapse responds to an action potential via the release of neurotransmitters. Unlike the electrical synapse, a chemical synapse does not have intercellular continuity across the synaptic cleft (Fig. 1b). When neurotransmitters that randomly diffuse across the gap junction are received at the receptor sites on the post-synaptic neuron, ion channels open to allow an inflow of sodium ions that in turn raise the membrane potential of the post-synaptic neuron. Due to the lack of direct transmission paths between the pre- and post-synaptic neurons, the response of a chemical synapse is much slower compared to the electrical counterpart.

Biological synapses modulate the flow of signals across the biological neural network and are believed to play the role of memory formation in the learning process [40]. A strong synaptic connection between two neurons allows almost the entire action potential from the pre-synaptic neuron to be transmitted to the post. On the other hand, a weak synaptic connection suppresses the impact of an action potential on the post-synaptic neuron. Here, we outline a widely accepted theory, known as Hebbian learning rule [56], that stipulates how the synaptic strength between neurons evolves during the learning process. This rule has thus far closely guided efforts in neuromorphic device development and may be summarized as follows. If a post-synaptic neuron fires a voltage spike after the pre, the latter is said to have directly influenced the depolarization of the former, and the synaptic strength is increased according to the time delay (Δt) between the two firing events (Fig. 1e). The increase is most significant when $\Delta t \sim 0$, i.e., the post-synaptic neuron fires almost immediately after the pre. Conversely, the synaptic strength is reduced if the post-synaptic neuron fires before the pre, i.e., $\Delta t < 0$. These synaptic changes linked to the relative timing difference in the firing of the pre- and post-synaptic neurons are widely coined as spiking-time dependent plasticity (STDP) [57-66].

When consecutive firing of pre-/post-synaptic neuron, also may refer as excitatory/inhibitory spiking events happens, the synaptic response of STDP would simplify to long-term potentiation (LTP) or depression (LTD) shown in Fig. 1f, respectively for excitatory or inhibitory events. In 1992, Dan and Poo proved on biological neuromuscular synapses that immediate and long-time depression happens when the postsynaptic pulses alone or the pre-synaptic spike is asynchronous, whereas synchronous pre- and postsynaptic spike have no effects [59]. To be precisely, the synapse will be weakened if there are only post-synaptic spikes, or the pre-synaptic spikes happens only after the post-synaptic spikes. Such biological observation is then confirmed by Debanne *et al.* in hippocampal slice two years later [60]. Afterwards, it is also found in rat hippocampal neurons that LTP happens if repetitive post-synaptic spikes within 20 ms of the pre-synaptic activation [62].

Alternatively, when only one or a few such events happen, the STDP rule will simplify to short-term potentiation (STP) or depression (STD), as shown in Fig. 1g, which shows the change from rest potential to action potential and back to rest potential on neuron membrane, without persistent change in the synaptic strength. Therefore, the major difference between short-term potentiation/depression and long-term potentiation/depression lies in whether the synaptic plasticity is permanently changed during the spiking activities.

3. Strategies in Current Transition Towards Neuromorphic Computing

ANN and SNN

As the assembly between terms used in existed ANN, including DNN, DCNN, *etc.*, and emerging SNN, a clarification between which should be addressed. Although as the name suggests, artificial neural networks include any neural network that is man-made, however, it should be made clear, as it has been introduced that SNN distinct itself as the third generation of ANN because of its time-dependent spiking computational unit [18]. Herein, in the context of this review, any artificial neural networks that are not spiking neural networks will be concluded as (traditional) ANN, and we separate SNN for the ease of discussion. Fig. 2 adapted from ref. [67] elucidates the difference well. As shown in Fig. 2a, the inputs of ANN are usually a vector ***X***, with a vector weight gain ***W*** by synapse multiplicator, then integrated and activated to generate the output. The inputs of SNN, however, are unipolar time-dependent spike trains weighted by synapses and activated by neurons. The synaptic weighting and neuron activating in SNN leverage on STDP and LIF, respectively, as described in the earlier section. Further difference in implementation is then illustrated in Fig. 2b that by using STDP, the time-dependent unipolar trains in SNN are interpreted to the analogue weights stored in the synapses and then used for exciting or inhibiting the post-synapse neurons, in clear comparison to the ANN method that uses discrete numbers stored in the digital memory and computed by arithmetic logic unit in processor for countless multiply-and-accumulate (MAC) operations, followed by a non-linear activation for the final result.

Neuromorphic computing is a general summary of the electronic implementation of human-brain inspired computing. In the context of this review, neuromorphic computing, however, only refers to the SNN implemented by emerging synapse and neuron devices. Because the ANN has diverged from perceptron so much that there is no assembly to the biological neural networks except for some terms borrowed, as we have illustrated in the above chapters. Furthermore, the physical level implementation of ANN and SNN shown in Fig. 2b made the statement more clear - The existing software-based ANN is performed entirely on processor with numerous data exchange between memory and processor, either or both of

 This journal is © The Royal Society of Chemistry 20xx

Please do not adjust margins

Please do not adjust margins

Fig. 2 ANN and SNN: Comparison and implementation. **a**, Computational unit of traditional ANN model and emerging SNN neuron model, where *W* denotes the synaptic weight, *X* denotes the input activation, *Σ* is the integration function, and *f* is the activation function. **b**, Implementation of ANN and SNN neurons. With the electronic implementation of ANN as current transition and emerging artificial neuron and synapse device implemented SNN as prospect. **Credits**: Adapted with permission from ref. [67], copyright 2019, Springer Nature.

which is bottlenecked in the current development. The hardware-based ANN enabled by in-memory computing (IMC) extenuates the load of memory, processor, and the bus between them, therefore reduce the power consumption, accelerate the speed, and ease the burden of IC design. However, the hardware-based ANN emulates the brain's functionality in a way that there is no clear distinction between memory and computing as the von Neumann architecture has. The basic operation assembles the software ANN, still. Hardware SNN uses artificial neuron and synapses as basic computational unit, in the most distinctive way that no actual numbers are passed between any part of the network except for unipolar spikes generated by neurons, which is the exact emulation of the biological neural network.

Hardware ANN: In-Memory Computing

Although they do not yet yield a complete neuromorphic system, in recent years, various notable hardware-based ANN approaches have been proposed for addressing the as-described von Neumann bottleneck [68-71]. These approaches are primarily aimed at boosting computational speed (thus data throughput) by performing MAC, typical unit of the CNN algorithm, within the memory storage. Known as IMC approach, or vector-matrix multiplication (VMM) machine shown in Fig. 3 a-b, this computational method reduces the transfer of data between the processor and memory. For example, Sony's IMX500 intelligent vision system [72], announced in mid-2020, is a systems-in-package AI-vision solution that features a CMOS image sensor stacked on top of a digital signal processor customized for performing computation within the SRAM. The product offers two operational modes; a high-resolution picture mode for human viewing and an AI inference mode where the image is down sampled and analysed using MobileNet at ~3 ms per frame [72]. Li *et al*. proposed an analogue spectrum analyser [73] with resistive random-access memory (RRAM) array. The input voltage signal with different frequencies (Fig. 3c) after multiplication with the conductance weights in the array could be transformed to a current signal that passes in certain cells (Fig. 3d). They performed 2D - discrete cosine transform (2D-DCT), an image processing/ compression method to rearrange the pixels in frequency domain, with their VMM machine to encode the image (Fig. 3e) and compare with the software (Fig. 3f), in which the distortion to human perception is negligible. Zidan *et al.*, using a similar strategy, implemented an RRAM-based analogue Poisson equation solver [74]. Likely, Oh *et al.* used RRAM to perform MAC and used Mott activation neurons [75] to emulate rectified linear unit (ReLU) activation function to achieve edge detection of image.

Another IMC approach, proposed by Yao *et al*. [68], leveraged on the multiplicative and additive nature of Ohm's law and

Please do not adjust margins

Please do not adjust margins

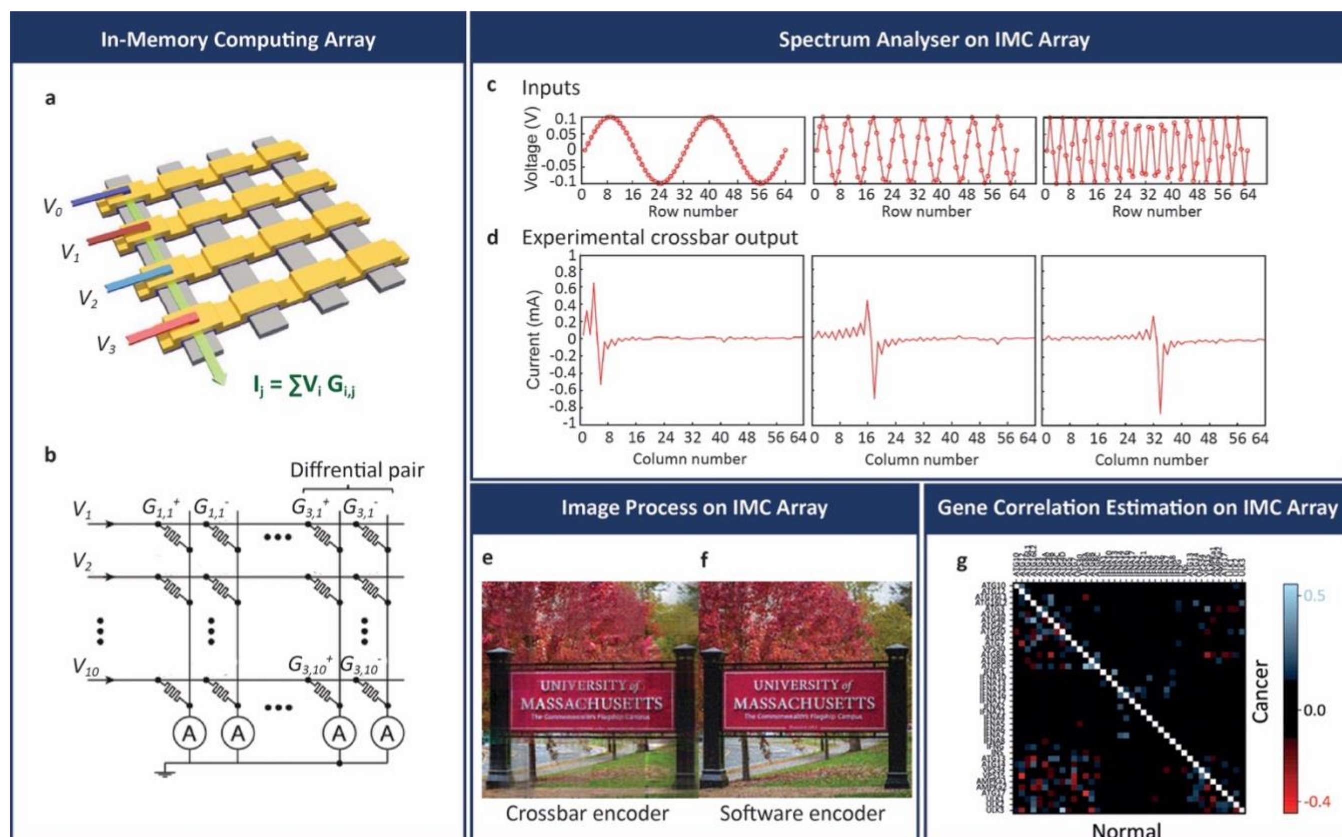

Fig. 3 In-memory computing using RRAM array. **a**, Schematics of RRAM array. The output current is the sum of several channels of voltage times the corresponding node conductance. **b**, Schematics of array with differential pair, where the differential output makes the array more robust. **c-f**, Spectrum analyser using RRAM array based on differential VMM, where with the input voltage signal (**c**) times the pre-programmed array weights, the array can output current at respective column expressing the frequency component of the input signals (**d**). With the functional hardware spectrum analyser, image encoding (two-dimensional discrete cosine transform, 2D-DCT) using RRAM array (**e**) in comparison to the software encoder (**f**). **g**, Gene correlation estimation on IMC array. Partial correlation computed of 40 genes for cancer and normal tissues (only displayed correlation greater than 0.13 for visualization reason). **Credits**: a is reproduced with permission from ref. [74] , copyright Zidan *et al.* 2018 Springer Nature; b is reproduced with permission from ref. [69], copyright Prezioso *et al.* 2015 Springer Nature Limited; c-f is reproduced with permission from ref. [73], copyright Li *et al.* 2018 Springer Nature; g is reproduced with permission from ref. [77], copyright Gallo *et al.* 2018 Springer Nature .

Kirchhoff's current law, respectively. It deployed a crossbar array of resistive memory cells wherein MAC computation was carried out. In an RRAM cell, the resistance or conductance of a sandwiched insulator layer can be modified electrically, and the change is usually rendered non-volatile for storage application. In Yao's work, the resistances of RRAM cells in each crossbar array denoted the optimized weights of a CNN kernel derived from offline training. Image pixels were converted to corresponding voltages and applied to the RRAM cells to realize the CNN convolution, with the result represented by the summed current of the array. The computational performance was benchmarked against Telsa's V100 [76] GPU and more than two orders of magnitude better power efficiency, and one order of magnitude better performance density were observed.

While most IMC applications focused on image processing, some unleashed MAC ability for the linear and partial equation solver. For example, Fig. 3g shows Gallo *et al.* work on 1 million PCM devices for linear equation solver and used it for partial gene correlation estimation in studies of cancer and normal tissues.

Admittedly, there are far more simulation works using RRAM for IMC than using physical array. However, the physical system is rather realistic, complicated, and interested. Here, in addition to the above-mentioned works, Table 1 summarized some of the on-array implementation of IMC using RRAM and FLASH and maybe for the future inspirations.

Table 1 Summary table of on-array in-memory computing approaches and their applications.

Works	Array size	Array type	On-array IMC (MAC/VMM) application
Berdan *et al.* [70]	5 × 5	Passive	Linear multiplicator
Zidan *et al.* [74]	16 × 3	Passive	Poisson equation solver
Li *et al.* [73]	128 × 64	1T1R	Spectrum analyser for image compression
Oh *et al.* [75]*	32 × 32	Passive	Activation neuron for edge detection
Sheridan *et al.* [78]	32 × 32	Passive	Sparse encoding
Yao *et al.* [68]	128 × 8	1T1R	Hybrid CNN
Guo *et al.* [79]	785 × 128	NOR-FLASH	MNIST classification
Yu *et al.* [80]	16 Mb	1T1R	MNIST classification
Burr *et al.* [81]	500 × 661	2-PCM	MNIST classification
Gallo *et al.* [77]	512 × 2048	1T1R	Linear equation solver for partial correlation of genes estimation

* Size for Mott activation neuron. The edge detection was implemented by cooperating 32 × 32 Mott neuron with 16 × 16 RRAM synapses.

This journal is © The Royal Society of Chemistry 20xx

Please do not adjust margins

Please do not adjust margins

While current innovative means of boosting computational speed have yielded substantial improvement over the cloud- and GPU-based approaches, data sampling, movement and computation are still being controlled by a central clock speed, like those in a von Neumann system. This operational mode differs entirely from that of biological neural networks in the brain, which process sensory data in an asynchronous spike-driven manner, i.e., computations are triggered by changes in the data themselves. To attain the speed and energy efficiency of the biological counterpart, man-made systems must adopt similar architecture and operating principle. A major research effort has been underway for nearly a decade to develop compact and low-power building block devices to realize this goal.

4. Neuromorphic Building Block Devices

Building block devices for a neuromorphic computer must exhibit the basic characteristics of biological neurons and synapses. For the artificial neuron, the internal variable must progressively build up according to the rate of the incoming voltage spikes and gradually dissipate in the absence of such spikes (i.e., the device should display a short-term memory). As for the artificial synapse, the internal variable must exhibit a continuum of non-volatile states that mimic the plasticity behaviour of the biological counterpart. Due to the significantly higher number of synapses ($\sim 10^{15}$) compared to neurons ($\sim 10^{10}$) in the human brain, size and energy consumption of artificial synapses are other key considerations that cannot be ignored in our drive towards a brain-like computer. In this section, we review some promising candidates, including valance changing memristor (VCM), electrochemical metallization memristor (ECM), interfaced-controlled memristor (ICM), charge-trapping memristor (CTM), phase change memory (PCM), spin-transfer-torque memory (STTM), and ferroelectric tunnel junction memory (FTJM), with their pros and cons.

A. Memristor

First predicted by Chua in 1971 [82] but largely disregarded until the successful experimental demonstration in 2008 [83], the two-terminal memristor is the fourth fundamental electrical component besides the capacitor, resistor, and inductor [82]. A key characteristic of the memristor is the current-voltage hysteresis loop, which gives it a non-volatile resistance memory property. The memristor can be "programmed" to at least two distinct high and low resistance states (HRS and LRS), with numerous intermediate states possible through controlling the applied stimulation [83]. Coupled with its structural simplicity which enables ultrahigh integration density in the form of a crossbar array, the memristor has been intensively studied in the past decade both as a resistive switching memory or RRAM for post-flash tera-bit memory application and an artificial synapse/neuron for neuromorphic computing. The idea of memristors mimicking the dynamics of ion channels was theorized by Chua and Kang [84] in 1976.

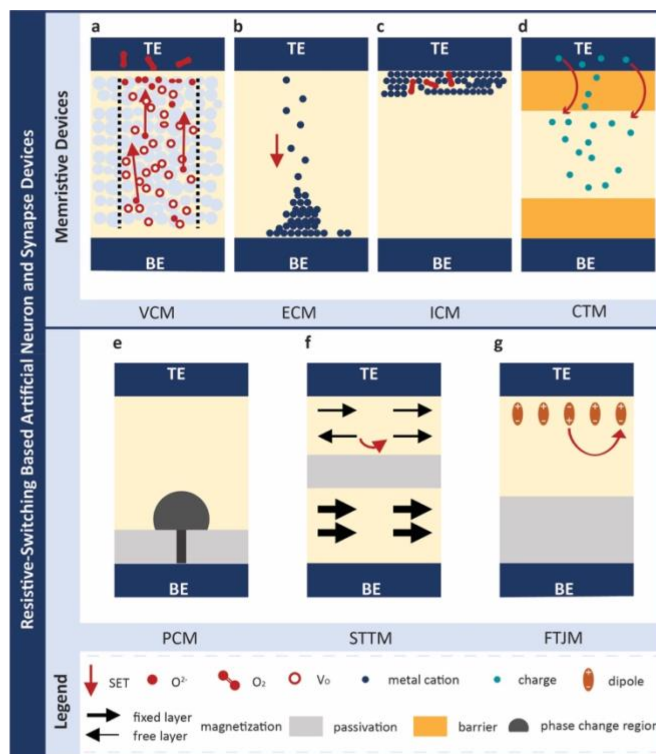

Fig. 4 Resistive-switching based artificial synapses and neurons. **a-f** are schematics of valance changing memristor (VCM, **a**), electrochemical metallization memristor (ECM, or namely conductive bridging memristor, **b**), interface-controlled memristor (ICM, **c**), charge-trapping memristor (CTM, **d**), phase changing memory (PCM, **e**), spin-transfer-torque memory (STTM, **f**), and ferroelectric tunnel junction memory (FTJM, **g**), respectively, where the red arrow indicates the set process. **Credits**: **a-g** are adapted from ref. [38, 85-92].

Since the experimental validation of the memristor concept by HP Labs in 2008 [83], many different memristive devices have been proposed and demonstrated (Fig. 4a-c). Generally, the physical mechanisms that govern resistance switching in these devices may be classified into the following categories, namely valance change memory (Fig. 4a), electrochemical metallization memory (Fig. 4b), interface-controlled memory (Fig. 4c), and charge-trapping memory (Fig. 4d).

Valence-change memristor

In 2008 the memristor predicted by Chua was first confirmed and built [83]. A valence-change memristor is typically made up of a sub-stoichiometric transition metal oxide (e.g., HfO_x [85, 93-112], TaO_x [74, 104, 107, 113, 114], TiO_x [114, 115], AlO_x [97, 100, 101, 104, 106, 116], NiO_x [117], etc.), and requires an electroforming step to create a filamentary conducting path, comprising oxygen vacancy defects, within the oxide network with the electrodes typically non-active metals. Subsequent resistance switching is ascribed to oxygen anion (O^{2-} anion) exchange between the filament and an adjacent active electrode [85, 93, 118, 119] (i.e., one that functions as an oxygen reservoir). A negative voltage applied to the electrode drives O^{2-} anions towards the filament and re-oxidizes part of it, creating a thin oxide barrier between the electrode and the remaining filament. This resets the resistance to a higher value (HRS). Conversely, a positive voltage induces across the thin re-oxidized layer a large electric field that regenerates the vacancy defects, setting the resistance to a lower value (LRS).

Please do not adjust margins

Please do not adjust margins

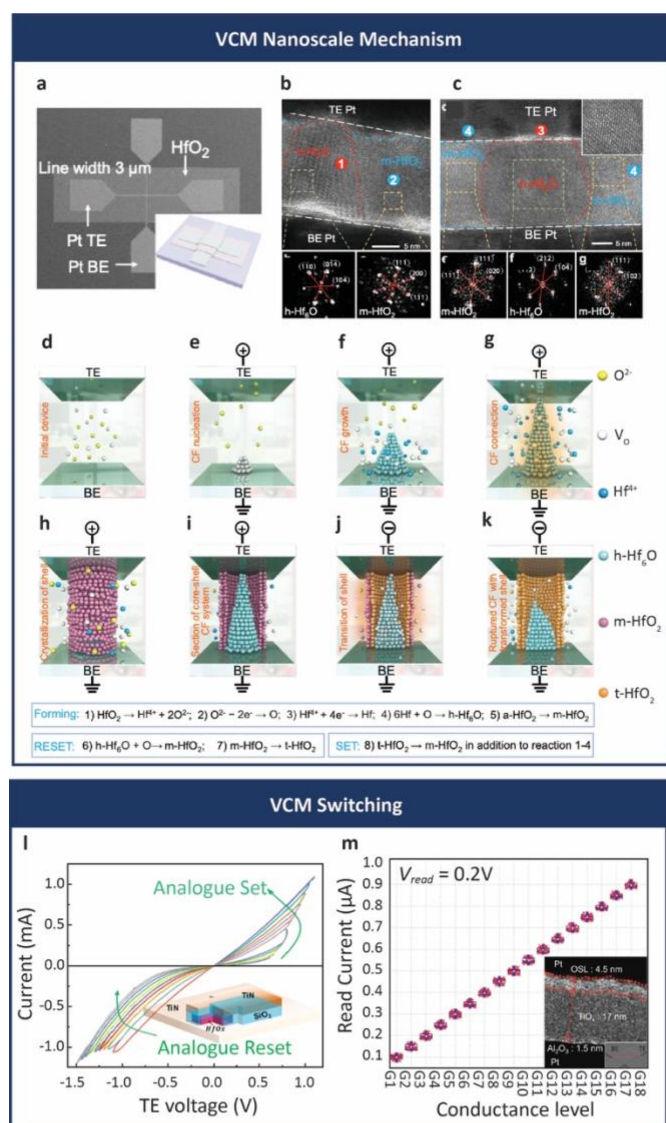

Fig. 5 VCM Nanoscale mechanism and switching for neuromorphic applications. **a**, Device SEM image and schematic. **b-c**, High resolution transmission electron microscopy (HRTEM) image of device operated under 0.1 mA and 1 mA compliance current, respectively. **d-k**, Illustrations of the evolvement of conductive filaments from forming to rupture. **l**, Typical analogue set and reset cycle of VCM devices for neuromorphic applications. **m**, Multiple conductance levels achieved by VCM devices for neuromorphic applications. **Credits**: **a-k** are reproduced under CC-BY licence from ref. [128], copyright Zhang *et al.* 2021 Springer Nature; **l** is reprinted from ref. [98], copyright 2020 American Chemical Society; **m** is reproduced under CC-BY licence from ref. [115], copyright 2022 Wiley-VCH.

Zhang et al. used high-resolution transmission electron microscopy (HRTEM) to capture the filament evolution of a $Pt/HfO_2/Pt$ VCM device shown in Fig. 5a. Fig. 5 b-c shows HRTEM image (with fast-Fourier Transform (FFT) diffraction patterns) of devices operated at 0.1 mA compliance and 1 mA compliance, respectively, where crystalline hexagonal-Hf_6O (h-Hf_6O) is believed to in the oxygen deficient conductive filament region and m-HfO_2 to be the shell of the filament. To illustrate, Fig. 5d-k shows the evolvement of h-Hf_6O filament from pristine state (Fig. 5d) to be formed (Fig. 5e-g), shelled (Fig. 5h-j), and ruptured (Fig. 5k). The detailed mechanism, restricted by the scope of this work, may not be well elaborated. Dittmann *et al.* reviewed the VCM mechanism in details [120] where the engaged audience should refer to.

Many works present excellent analogue switching performance in D.C. mode without [95, 98, 99, 121] or with [94, 96, 97, 100, 101, 109, 114, 116] the help of compliance current, as shown in **Fig. 5l**. However, during set, the current usually increases abruptly due to heating that in turn accelerates defect generation [113, 122, 123]. To suppress the thermal runaway, a series resistance that limits the current surge is required. This may be fulfilled by a selector device, typically a transistor, which also helps eliminate the sneak-path current problem in a crossbar array, which will be discussed in the following section. On the other hand, the current decreases gradually during reset because the migration of the O^{2-} anions would be self-limited by the increasing thickness of the re-oxidized layer adjacent to the electrode [107, 124]. Sometimes, an oxygen reservoir layer [99, 105, 106, 108, 109, 111, 112, 115-117, 121], thermal enhance or electro-thermal modulation layer (TEL/ETML) [68, 104, 107, 125-127] is adopted to mitigate such abrupt set behaviour. As shown in Fig. 5m, Kim *et al.* [115] reported an alumina VCM device with TiO_y ($y = 1.81$) overshoot suppression layer (OSL) (inset shows its TEM image) and showed a conductance modulation within 20 nA error tolerance for 70 cycles.

Electrochemical metallization memristor

This memristor, also known as a conductive-bridging random access memory (CBRAM), relies on the formation and dissolution of a metal filament as the mechanism for resistance switching (Fig. 4b) [129]. The metal electrode used is typically silver (Ag) or copper (Cu), which exhibits high diffusivity in most solid electrolytes [130, 131]. A positive voltage applied to the Ag electrode ionizes the Ag atoms, and the cations then drift under the electric field towards the counter electrode where they are reduced, forming a microscopic Ag "hillock" that serves as a virtual electrode for subsequent reduction of Ag^+ cations [129, 132, 133]. A set occurs when the Ag filament extends back and connects the anode. A negative voltage reverses the process by driving Ag^+ cations back to the Ag electrode, causing a reset. Lyapunov *et al.* demonstrated the diffusion of Ag ions clearly under *in-situ* TEM, shown in Fig. 6a-d [134]. During negative bias, the Ag diffused out of the GeS layer (a-b-d-c). While for the fresh device that has not undergone the formation of Ag filament, the device is able to self-relax to its fresh state (c to a), as further illustrated in Fig. 6e. The main disadvantage of this device is that the resistance switching during both set and reset are abrupt, thus might limit synaptic application to binary neural networks [135-138], while recent work by Abbas *et al.* on WTe_2 based device shows gradual reset with long retention[139] and work by Wang *et al.* on HfO_x/AlO_y super-lattice-like (SLL) device shows controllable analogue set and reset[101] may relief the issue.

Besides non-volatile switching, volatile or threshold switching is observed when the set current is capped below a certain value (usually on the order of microampere) [140, 141]. In this case, the LRS is maintained over a limited voltage range only. When the voltage is decreased below a threshold value, the device reverts automatically to the HRS. The volatility is believed to stem from a relatively thin Ag filament formed under a limited set current [143]. Further, a more comprehensive review by Abbas *et al.* on

This journal is © The Royal Society of Chemistry 20xx

Please do not adjust margins

Please do not adjust margins

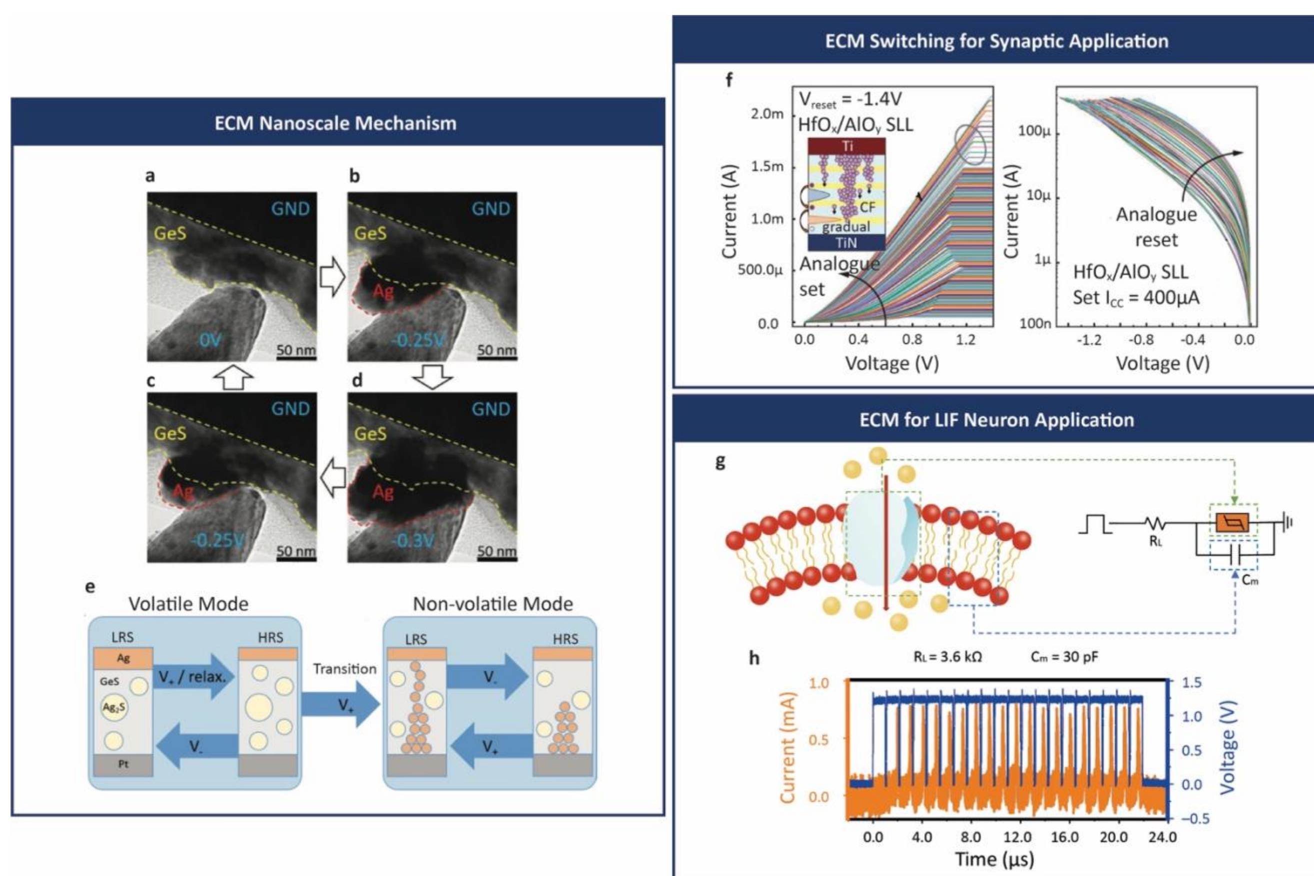

Fig. 6 Electrochemical metallization memristor. **a-d**, *In-situ* TEM image showing Ag ions diffusion under negative bias. **e**, Illustration of the set/reset process of GeS ECM device. **f**, Analogue switching for synaptic application of HfO_x/AlO_y super-lattice-like (SLL) device. The analogue set is by setting different compliance current while the analogue reset is accomplished by setting different reset voltage. **g**, Biological LIF neuron emulated by ECM with circuitry. R_L and C_m denotes load resistor and membrane capacitor, respectively. **h**, Artificial LIF neuron response (current) to the input spikes (voltage). **Credits**: **a-e** are reproduced with permission from ref. [134], copyright 2022 Kim *et al.* Wiley-VCH GmbH; **f** is reproduced with CC-BY licence from ref. [101], copyright Wang *et al.* 2022 Wiley-VCH GmbH; **g-h** is reproduced with CC-BY licence from ref. [142], copyright Duan *et al.* 2020 Springer Nature.

ECM elaborated it well and accurately, which helps the understanding of this kind of device [143].

Due to the high solubility of Ag, the thin filament readily “dissolves” when the excitation voltage is reduced. Exploiting this characteristic, several works [142, 144, 145] made use of this behaviour to implement the integrate-fire function of a neuron. The circuit comprises a capacitor connected parallel to the threshold switch. When the capacitor is charged by input spikes to a voltage higher than the set voltage, the switch transits to the low-resistance state and discharges the capacitor. As the capacitor voltage decreases below the threshold, the switch transits back to the high-resistance state. The momentary discharge of the capacitor produces an output current spike. Duan *et al.* [142] takes this approach further by connecting 4 of such LIF neurons to 1 synaptic device to emulate the biological neuron and synapse illustrated in Fig. 15h.

For the synaptic operation, tuneable long-term potentiation and depression by varying spike amplitude [69, 146], spike number [147], and spike rate [141] are reported using non-volatility of ECM. With volatility, ECM shows also tuneable short-term potentiation by varying spike amplitude [134, 146], spike rate [134], and spike number [134]. It is worth mentioning that on behavioural level, ECM device is able to emulate Pavlov’s dog experiment in simulation and can be developed to an addiction inhibition machine [148] thanks to its easy transition between volatile and non-volatile switching.

With the volatile switching characteristics, or sometimes refers as threshold switching (TS), ECM devices may be adapted for LIF neuron application, as illustrated in Fig. 6g. The biological neuronal membrane is emulated by the parallel capacitor (C_m) and the biological ion channel is emulated by the TS device, which shares more similarity to the conduction mechanism of ECM. Duan *et al.* used such device with load resistor and capacitor showing LIF neuron characteristics discussed above in Fig. 6 h[142] and they also applied neuron-synapse system for SNN simulation, of which more details will be discussed in the following sections.

Interface-controlled memristor

Interfacial resistive memory is a distinct type of memristor that modulates device conductance by forming an oxide layer between the electrode and dielectric layer, rather than by forming a conductive filament via redox reaction or oxygen vacancy movement. Due to the lack of conductive filaments, it is also known as non-filamentary memristor. The switching materials typically used in interfacial resistive memory are $Pr_{0.7}Ca_{0.3}MnO_3$ (PCMO) [86, 149-155] and TaO_x with TiO_2 [88] or Ta_2O_5

Please do not adjust margins

Please do not adjust margins

[156]. PCMO was first introduced as a resistive-switching material in 2009 [86]. The resistance switching behaviour of interfacial devices is attributed to the formation of a thin oxide layer at the interfaces between the electrode and PCMO or oxygen vacancy rich materials. As proposed by Wang *et al.*[88], a negative bias would drive oxygen ion (O^{2-}) away from the described interface and thus increases the effective barrier width of the electron conduction, as illustrated in Fig. 7a. Further band diagram calculation in Fig. 7b shows that the conduction of Ta/TaO_x interface is modulated by the tunnelling of the barrier for LRS device under negative bias. Reversely, a positive voltage drives oxygen ions towards the Ta/TaO_x interface, subsequently reduce the effective barrier width. In the meantime, as shown in band diagram in Fig. 7c, the modulation layer at positive bias is relocated on TaO_x/TiO_2 barrier, which results in lower resistance. Similar observation is confirmed in Mo/PCMO devices by Moon *et al.* [153]. Park *et al.* used N-rich TiN/PCMO device to achieve gradual DC switching, thus with further linearity ability for neuromorphic computing applications [154]. Interface-controlled memristors were first introduced in 2013 as a neuromorphic device, and early-stage research has shown their capability of better linearity in LTP and LTD [149-154]. Lashkare *et al.* also emulated artificial neuron with PCMO ICM with good firing energy control (212 pJ). Consequently, many simulations based on interface-controlled devices have been conducted to achieve spiking neural network (SNN)-based face recognition [150], pronunciation classification [149], and time-dependent signal prediction [150].

Charge-Trap Memristor

Like charge-trap transistors commonly used in flash memory, switching of charge-trap memristors (CTM) leverages on the charge trapping and de-trapping of the charge trapping layers of the device. Typically, two barrier layers sandwich a trapping layer are required for CTM, shown in Fig. 8a as an example, in which device Kim et al. investigated in a comparative study [92]. They discussed devices missing Ta_2O_5 layer which suffers from LRS fail in retention and the ones missing Al_2O_{3-x} layer which suffers from HRS fail in retention and concluded with the

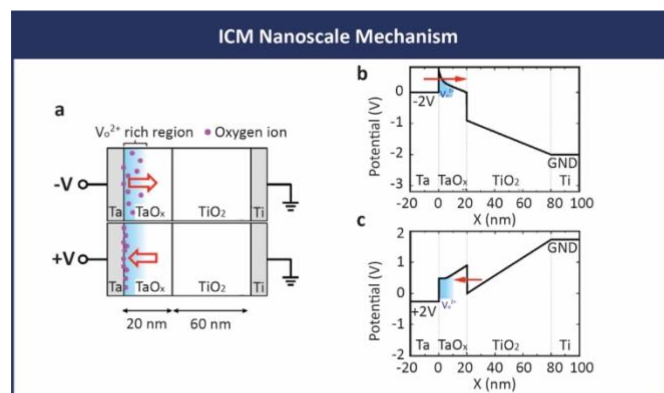

Fig. 7 Interface-controlled memristor. **a**, Illustration of the switching mechanism explained by homogeneous barrier modulation model: Oxygen ions migrate away from oxygen vacancy rich region at Ta interface with negative bias (reset) increasing the effective barrier width for electron conduction and migrate towards that region with positive bias (set). **b-c**, Energy band diagram in LRS calculated at -2V and 2V read bias, respectively. **Credit**: Reproduced with CC-BY licence from ref. [88], copyright Wang *et al.* 2015 Springer Nature.

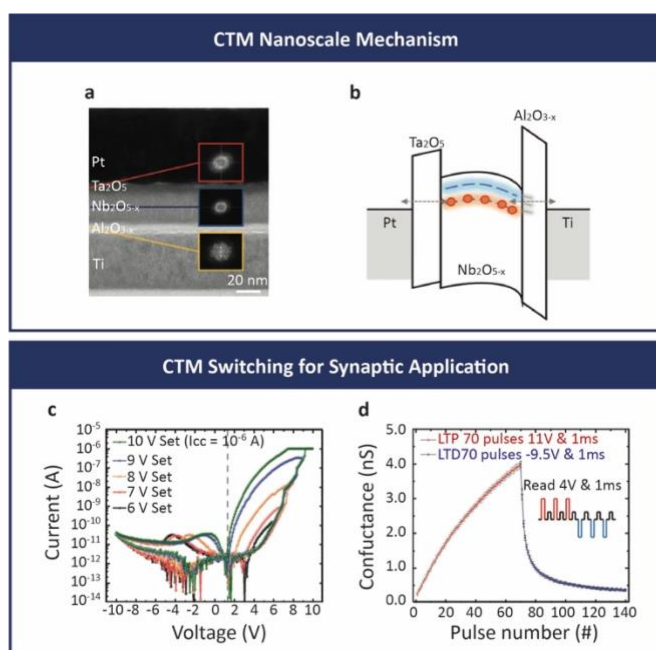

Fig. 8 Charge-trap memristor. a, Cross-sectional TEM image of the Pt/Ta_2O_5/Nb_2O_{5-x}/Al_2O_{3-x}/Ti device. Inset: FFT image of each dielectric layer. **b**, Schematic energy band diagram shows charge trapping mechanism of CTM. **c**, Multi-level analogue set/reset. **d**, LTP/LTD emulated by CTM device. **Credit**: Reproduced with CC-BY licence from ref. [92], copyright Kim *et al.* 2023 Wiley-VCH.

illustration as Fig. 8b, that aluminium oxide helps with buffering Ti diffusion whereas tantalum oxide stops spontaneous de-trapping. Although charge-trap transistor is widely investigated and used, CTM, however, draws attention only until recent years for its potential of higher memory density as compared to flash, low operating current, forming free, and self-compliance characteristics [92, 157-160]. Recently, Kim et al. vitalized CTM as neuromorphic device by showing its good analogue set (Fig. 8c), LTP/LTD (Fig. 8d), and excellent 8-bit retention proving its potential in IMC applications [92].

Inherited from charge trapping mechanism, high programming voltage (~10V) might be one of the major obstacles in the neuromorphic application, which shall be enhanced in further studies.

B. Phase-Change Memory Device

As the name suggests, phase-change memory (PCM) depends on thermally induced transition between the crystalline and amorphous phase as the mechanism for non-volatile resistance switching (Fig. 4e). A material widely studied for phase-change memory application is germanium-antimony-tellurium (GeSbTe or GST) [161], by virtue of its ease of fabrication and low phase transition temperature. Meister *et al.* employed the *in-situ* TEM showing the resistance change in the nanoscale level of a GST PCM device depicted in Fig. 9a [162]. Shown in Fig. 9b that in the crystalline phase, GST has a low electrical resistance. Under short high-current pulsing, GST can be transformed into an amorphous phase having a much higher resistance (Fig. 9c), i.e., reset of the PCM device. Selected area diffraction (SAD) of the red circle regions was carried out to confirm the polycrystalline and amorphous phase, shown in Fig. 9d-e, respectively. Reversal to the low-resistance crystalline phase or the set

This journal is © The Royal Society of Chemistry 20xx

Please do not adjust margins

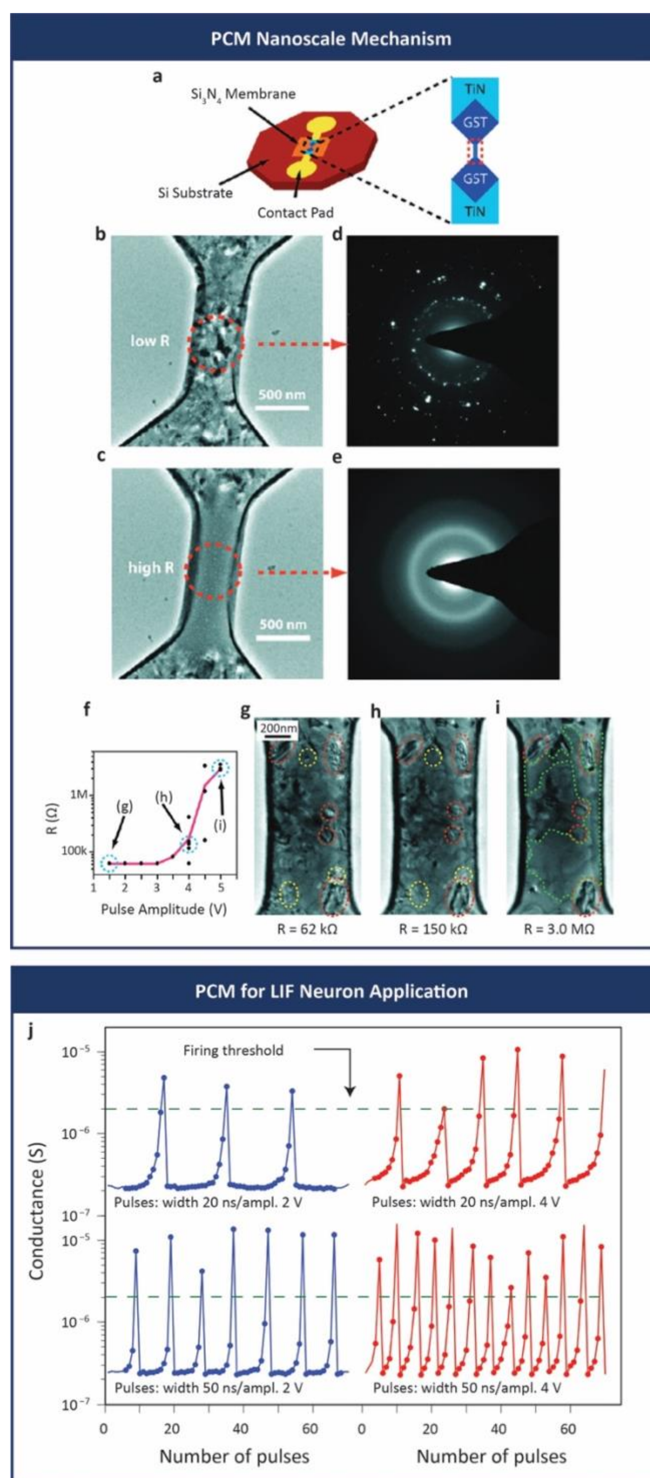

Fig. 9 Phase-change memory device: Nanoscale mechanism and LIF neuron application. **a**, Device structure illustration. **b** and **c**, in-situ TEM image of PCM device in LRS and HRS, respectively. **d** and **e**, Selective area diffraction (SAD) image of the circled region confirming the amorphous and polycrystalline phase of b and c. **f**, Device reset by 400 ns varying amplitude voltage pulse, at which the TEM images of the device are shown in **g-i**, confirming the crystallization phase by the reset voltage pulse. **j**, PCM device used for artificial neuron. Figure shows spiking rate and amplitude dependency of the neuron firing. **Credits**: a-i are reprinted with permission from ref. [162], copyright 2011 American Chemical Society; j is reproduced with permission from ref. [173], copyright Tuma *et al.* 2016 Springer Nature Limited.

process may be realized using a lower current pulse or a voltage pulse but applied over a longer period. Shown in **Fig. 9f**, by applying 400ns varying amplitude voltage pulses, the device resistance changes gradually, which was further examined by TEM showing in Fig. 9g-i at the respective points, confirmed the transition from amorphous phase to crystalline phase during reset. In ref. [87], Wong et al. reviewed more basics and theories of phase change materials and devices to understand the mechanisms of PCM.

Through modulating thermal energy input, a gradual transition that yields multiple resistance states can be achieved, which has been exploited for synaptic emulation by numerous studies [163-171], where Suri *et al.* and Kuzum *et al.* are the first to use PCM as artificial synapse [163-168]. Thanks to PCM devices' gradual phase transition by Joule heating effect and stable phase physics, PCM shows great potential in multi-bit storage with long retention time. This stability gives many benefits in long term memory: PCM synapses show excellent tuneable LTP by adjusting voltage or current pulse width [166, 168], amplitude [171, 172], and rate (duty cycle) [165-167]. Tuma *et al.* also used PCM device for artificial neuron application, as shown in Fig. 9j. The artificial LIF neuron shows tuneable firing rate depending on the spiking rate and amplitude.

However, the phase change induced by Joule heating effect is non-linear. A typical milli-seconds to seconds interval between set pulses is adopted to prevent over-heat with pulses [163, 166, 167, 170, 174], which is detrimental to the high-speed operation of the device. Another problem brought together by Joule heating is the power consumption that despite the fact that the technology node of PCMs has shrunk down to 40 nm diameter [172], the action energy consumption for pulse operation touches the bottom at pico-Joule level [87, 163, 165, 170-172].

C. Spin-Transfer-Torque-Based Device

As a type of magnetic random-access memory (MRAM), spintronic device emerges as a potential candidate for emulation of neurons and synapses [175]. The major difference between MRAM and non-MRAM is the storage media: The magnetic memory uses magnetization for the data storage while the non-magnetic memory uses electrons or defect states. Shown in Fig. 4f, the typical structure of spin-transfer torque cell is a sandwiched structure of one non-magnetic layer in between two nanomagnetic layers, of which one layer has fixed magnetization $\mathbf{M}_{fixed}$ and the other has free magnetization $\mathbf{M}_{free}$. When the current is injected into the stack, the spin torque will rotate $\mathbf{M}_{free}$ and thus through the magnetoresistance effect change the resistance of the device [89]. Spin torque can either rotate $\mathbf{M}_{free}$ towards or away from $\mathbf{M}_{fixed}$, depending on the polarity of input current, whose density also determines the amplitude of spin torque [176, 177]. Ideal value of input current is $\sim 40\mu A$ under 22nm CMOS technology [178]. Parallel state (P state) is hence achieved when magnetizations of free layer are paralleled with the fixed layer, and antiparallel state (AP state) is achieved by the versa. The SET and RESET processes are induced by sweeping positive and negative D.C. current, respectively. Since spintronic devices are magnetization based, it is not straightforward to include them in our benchmarking scheme. Therefore, we will discuss briefly the merits and challenges here. For the audiences who are

Please do not adjust margins

engaged in this field, here suggests a detailing review on neuromorphic MRAM by Shao *et al.* [179].

In 2014, Vincent *et al.* [180, 181] used spintronic memristive device to simulate neuromorphic computing ability. It is found that spintronics has stochastic switching [180-184] and transiting [185, 186] nature, so the device functions binarily. Recent reports proposed novel-structured spintronic devices [187, 188] to achieve continuous potentiation/depression by tuning hall resistance.

From the discussion in device physics, the biggest merit of MRAM lies in its non-volatility, i.e., long retention, high endurance, and compatibility for front-end-of-line CMOS fabrication [189]. Thus, commercialized MRAM chips have been fabricated [189] for its capacitor-less high-density potential. However, it is also reported that spintronic devices are inherently prone to bit errors due to thermal activations [175], consume large operating power [187, 188], use complicated structure [190], and require circuitry [191] or extra component [188] for the conversion between electrical signal and magnetic states, which may challenge the device application.

D. Ferroelectric Tunnel Junction Device

First discovered in 1920 [192], ferroelectricity is a phenomenon that the electrical polarization of the material can be reversed by applying an external voltage, showing a hysteresis curve. Ferroelectric materials are extensively demonstrated and commercialized in non-volatile random-access memory (NVRAM) [193-195]. As for artificial neuron and synapse applications, ferroelectric tunnel junction (FTJ) devices are introduced here. Shown in Fig. 4g, as the polarization of ferroelectric nanolayer changes, polarization charges effect induces asymmetrical barrier heights [196, 197]. While with the polarization points downward, the barrier height reduces to Φ_- (LRS) and the barrier height increases to Φ_+ when the polarization directs upward (HRS). Since tunnel transmission is determined by the square root of the barrier height, the junction resistance is hence dependent on the barrier height [91].

To investigate the switching in nanoscale mechanisms, Chanthbouala *et al.* employed the piezoresponse force microscopy (PFM) shown in the Fig. 10a during positive (red) and negative (blue) voltage sweeping. Starting from the LRS, the device shows homogeneously up-polarized states and gradually transits to mostly down-polarized states with PFM showing the nucleation and expansion of down-domains under positive pulses of increasing amplitude. Oppositely, negative pulses with increasing amplitude results in the nucleation and expansion of up-domains. Typical ferroelectric dielectrics used in FTJ in neuromorphic application are $BaTiO_3$ (BTO) [198-202], $BiFeO_3$ (BFO) [91, 203, 204], ferroelectric $Hf_{0.5}Zr_{0.5}O_2$ (Zr-doped HfO_2, FE-HZO) [205-208], and HfSiO (Si-doped HfO_x) [70]. For more ferroelectric materials and mechanisms, a rather interesting review by Mikolajick *et al.* may help with the understanding of ferroelectric, materials, and devices [209].

The first a BTO FTJ device reported by Chanthbouala *et al.* [198] exhibits a gradual switching with good on- to off-ratio (~10^3), shown in Fig. 10b. Their work also shows the device tuneable potentiation and depression ability by applying consecutive identical pulse trains varying the number of depression (Fig.

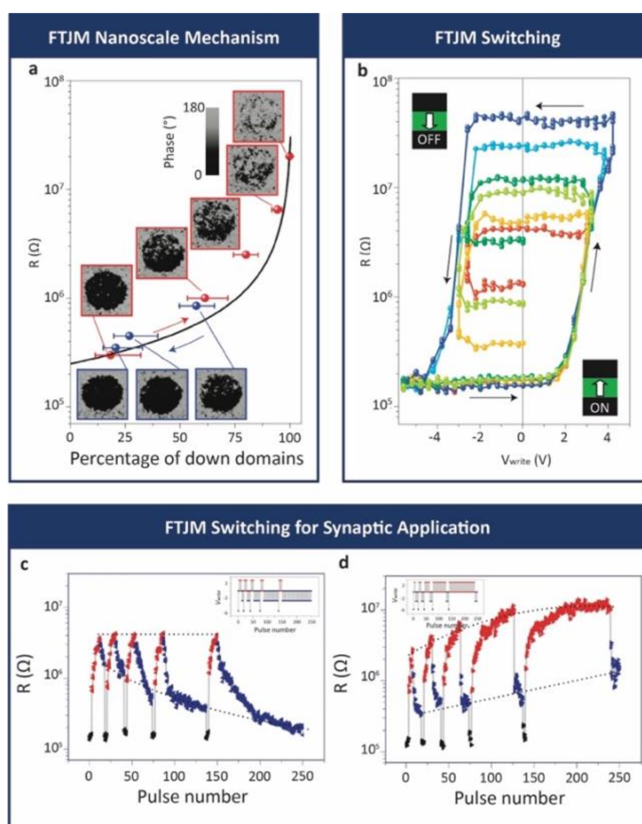

Fig. 10 Ferroelectric tunnelling junction device for neuromorphic application. a, Piezoresponse force microscopy (PFM) image captured during applying increasing positive (red) and negative (blue) voltage pulses. **b**, Tuneable FTJ device switching characteristics with different write voltage. And **c-d**, Tuneable FTJ potentiation and depression with varying reset pulse number (**c**) or set pulse number (**d**), where insets show the pulse scheme. **Credits**: Reproduced with permission from ref [198], copyright 2012 Chanthbouala *et al.* Springer Nature Limited.

10c) or potentiation pulses (Fig. 10d). Later, Ryu *et al.* [206] showed HZO FTJ device with gradual polarization change in hysteresis thus enabling a better potentiation and depression in synapse application.

E. Memcapacitor

Memcapacitor is recently reported [210] used for neuromorphic applications and has almost symmetrical and linear LTP/LTD. Physics of memcapacitor is rather simple: The capacitance of memory dielectric is modulated by the applied field in a 4-terminal structure. While memory dielectrics are commonly ferroelectric materials or charge trapping materials. With the appropriate programming gate voltage (memory window), the charges or fields are trapped or fixed in the dielectrics by a charge shield formed in the n^- region. The device states are read out from the bottom electrode when applying a biased alternating voltage on the gate [210]. However, the device needs complex circuitry to read out device states due to the capacitive nature. Also, benchmarking for this emerging type of electronics is not straightforward as compared to the resistive kind of device: although the capacitor consumes ideally no energy during the operation for it only involves with the storage of charges rather than electro-conduction, however, in the neuromorphic application, the energy carries by the spikes shall

 This journal is © The Royal Society of Chemistry 20xx

Please do not adjust margins

Please do not adjust margins

be stored, or consumed within the device to program the capacitive states. Therefore, the performance is similarly characterized as the rest of the devices.

5. Universal Benchmark of Artificial Synapse and Neuron Devices

So far, seven basic types of resistive switching-based electronic neuron and synapse devices and their switching mechanisms are discussed. Behind the obvious mechanism, devices perform differently: some with large switching ratio, some with faster switching speed, some with better potentiation/depression linearity, some requires large voltage, some requires long pulse intervals, some are flexible, some are CMOS-compatible while some are not, and so on. There is thus an urgent need for providing a benchmark that is straightforward and universal to locate the device by its performance intra- and inter- device groups. By considering the needs and the physics of emerging neuromorphic devices, we find the energy/power consumption become a suitable candidate for its universality, i.e., can be applied to any devices that require electricity to operate. Precisely speaking, we adopt the spike voltage (or current for some phase changing synaptic devices), LRS and HRS conductance, and spike timing used in spiking potentiation and depression for the energy and power benchmarking.

A. Benchmark for Artificial Synapse Devices

Benchmark for synapse devices is provided in Fig. 11a-b. To describe the data, the action energy and standby power are defined by the eq. 1 and eq. 2, respectively.

$$E_a = V_{spike}^2 \times \frac{G_{on}+G_{off}}{2} \times \tau_{spike} \text{ (eq. 1)}$$

$$P_s = V_{spike}^2 \times G_{off} \text{ (eq. 2)}$$

where E_a and P_s are the action energy in Joule and standby power in Watt, respectively. V_{spike}, G_{on}, G_{off}, and τ_{spike} are spike voltage in Volt, LRS conductance in Siemens, HRS conductance in Siemens, and spike timing (pulse duration) in Second, respectively.

Action energy

We introduce the concept of action energy, which is in correspondence to the action potential of the neuron membrane. Because the transition from LRS to HRS or vice versa is continuous with good linearity for most benchmarked devices, the arithmetic means of conductance is used in action energy instead of fitting each experimental result. For devices with large HRS/LRS ratio, it is easy to prove that the action energy is approximate to the energy consumption at LRS.

Standby power

The standby power metric measures the off power of the device. For the passive crossbar array configuration, the write operation will inevitably give a current flow between cells which consumes energy especially if the device has high HRS conductance. And it is particularly relevant in the context of a fully connected biological neural network. As an example, a Purkinje neuron may have as many as 1000 dendrites, which can further connect to 10,000 neurons [211]. The higher the standby power of the synaptic device, the higher the chance of misfiring, and the combined leakage current of 10,000 neurons can be disastrous.

Spike timing

In addition, we introduce the spike timing metric as a separate benchmarking tool. This is important to ensure the temporal dynamic range of the device. For traditional transistors, the operation frequency is always adopted as an important timing factor for both digital CMOS and analogue amplifier applications. Although the maximum frequency of digital IC now is greatly affected by circuit level design, the device maximum frequency still matters on the minimal timing that the device operation is intact, and the performance is not significantly compromised. Similarly, for synaptic and neuron devices, minimum spike timing matters for it determines the temporal dynamic range and together with the voltage, metrics by the action energy (the integral of amplitude as a function of timing), determines the spatial dynamic range of the devices. Thus, the smaller spike timing and lower the action energy the device can show, the smaller conductance it can be controlled by each individual spike, which helps with the overall performance of the array level application. If the spike timing is greatly compromised, there will be little room left for conductance modulation by multiple spikes, for example, 256 spikes (6-bit conductance) with each $\tau_{spike} = 1\ ms$ will take half a second to finish, in which case for the signal with high dynamic range, performance will be greatly affected.

Overall metrics and applications

Fig. 11b shows the metrics median comparison between VCM, ECM, ICM, and FTJM, with absence of CTM and mem-capacitor due to the limited number of reported synapse devices that may cause the biased statistics. Despite all these three metrics are expected to be as low as possible, it is very demanding to require all devices perform in this way. In Fig. 11b, we also suggest few application directions, including hardware SNN, in-memory computing (updating frequently), and DNN accelerator (updating rarely), if the device outperforms only part of the metrics, given the fact that CMOS transistors, even developed for decades, have lots of limitations, but were never impeded their application in computing chips. For synapse devices, they are expected to outperform in all metrics for hardware SNN implementation. As it can be concluded from the section III that SNN requires in-time synaptic weight updating, which requires low action energy and fast spike timing, as well as demands for low standby power because the number of neurons of one dendrite can connect can be extremely high, thus preventing too much power consumption during firing of the other neurons. In-memory computing, however, requires only faster spike timing and lower action energy for the frequent synaptic weight update operations. On the other hand, DNN accelerator, which already has its synaptic weight trained offline, rarely or never requires for the updates of synaptic weight, thus suitable for devices with low standby power.

Discussion

VCM devices are premier candidates for artificial synapse application for number of states up to 2048 states [212], long

Please do not adjust margins

Please do not adjust margins

Fig. 11 Universal benchmark for artificial synapse and neuron devices for valance changing memristive device (VCM), electrochemically metallization memristive device (ECM), interface-controlled memristive device (ICM), ferroelectric tunnelling junction device (FTJM), and mem-capacitor. **a**, Benchmark for synapse applications, where standby power is a function of action energy and the diameter of the bubble indicates the spike timing of the device. **b**, Overall performance comparison of artificial synaptic devices based on the median of each device group in the benchmark. The outer frame suggests possible neuromorphic application direction. **c**, Benchmark for neuron applications, where firing energy is a function of spiking energy. **Credits**: VCM data are extracted from ref. [94, 95, 97, 98, 100, 102-108, 114-116, 124-126, 213-220], ECM data are extracted from ref. [69, 122, 123, 220-228], ICM data are extracted from ref. [88, 149-154, 229], and FTJM data are extracted from ref. [70, 198, 200, 204-207, 230, 231], mem-capacitor data is extracted from ref. [210], artificial neuron data are extracted from ref. [142, 173, 232-243].

multi-bit retention up to 6000s for 3 bits (8 states) [213] and endurance up to 1 billion cycles [214]. VCM artificial synaptic devices consume low operational energy (median ~ 220 pJ) as well as low standby power (median ~ 34 µW), as shown in Fig. 11a, among the available data, some devices can suppress the energy consumption per average spike operation down to sub-pJ. The low energy budget ascribes to the following engineering: Introduction of vacancy migration barrier by multi-stacked layer

 This journal is © The Royal Society of Chemistry 20xx

Please do not adjust margins

Please do not adjust margins

($TiO_x/HfO_x/TiO_x/HfO_x$ structured reported by [94]) or alternatively, introduction of electro-thermal modulation (or namely, overshoot suppression) layer using TaO_x in ref. [104, 107, 125, 218] , TiO_x in ref. [115], or VO_x layer in ref. [214]. The merit by such engineering allows the spike pulse width of the above-mentioned devices to be significantly shorter thanks to the better control of the filament formation and rupture, which allows them speed up to 1 MHz to sub-GHz level when operates with CMOS-based processor. Moreover, the linearity of potentiation and depression is also much enhanced [101, 104, 115] for the additional benefit of better control of V_o and heat generation. However, besides common RRAM variation problems, spiking operation of VCM suffers from low action/standby ratio, which causes high standby power (in a range from microwatts to milliwatts, shown in Fig. 11b) as compared to non-RRAM devices. This is one of the reasons why selector-less passive array application for VCM is yet to be reported. Also, despite VCM devices shows promising characteristics like multi-states, long-retention, and high endurance, however, these properties are reported in separated devices. There is not yet any work showing a device have a collection of the promising features. The difficulty may lie in the instability and stochasticity of the oxygen vacancies [120]. It may require systematic studies to verify the coexistence of all these characteristics. And we encourage the future work on multi-states device to include the retention and endurance data, no matter excellent or mediocratic, to enable the further discussion in this regard.

Further analysis of ECM devices in Fig. 11a-b shows reasonable standby power (median ~ 56 µW) as compared to its worst action energy (median ~ 13 nJ) between classes. Despite ECM typically has bigger memory window, the high current used to stabilize the metal filament may cause a high action energy in the synapse application. However, efforts have been made to reduce the action energy to pJ level. Different from VCM, enhancement on ECM centres on the manipulation of cation conduction channel. Remarkably, ref. [225] uses 2 nm Mo/Ti or Ti barrier layer to buffer the diffusion of cation, reducing the action energy consumption to 2 pJ and similar cation barrier HfO_x/AlO_y superlattice-like structured device used in ref. [101] shown in the inset of Fig. 6f to lower the action energy to tens of picojoules. Additionally, the optimized anion migration helps greatly with the linearity in potentiation and depression to 1.44 and 2.55. Ref. [244] uses tellurium (Te), an elemental small bandgap semiconductor, as anode to reduce the 1-atom conductance from 80µS to 2.4µS and thus reduce the 1-atom program energy to 0.2 pJ and action energy for potentiation to 140 pJ. Similarly, ref.[122] uses less-diffusive tantalum (Ta) as anode which forms a more controllable conductive channel to make potentiation and depression fast to 100 ns spike to achieve better energy performance (81 pJ). Following this path, ref. [147] uses epitaxially growth SiGe in which a conduction channel enabled by dislocations can be selectively etched and widened to form an even better controlled conduction channel. By confinement of conduction channel in the selective-etched region, not only the standby power is suppressed to 1.5 µW, but also its cycle-to-cycle and device-to-device (different etching batch) variation is stressed to less than 1% and 4.9%, respectively. However, most device may suffer from high action energy to achieve a stable resistance state, from visualization in Fig. 11b. Thus, instead of trying for a viable candidate for synapse application, ECM suits better for neuron applications for its easy transition in volatility and assembly to biological neuron model, as described in Fig. 6g and will be covered in the following discussions.

For interface-controlled synaptic devices performance analysed in Fig. 11a, they have much lower action energy and standby power than valance change or electrochemical metallization devices. This is attributed to the low action/rest current of the device stack, which forms no conductive channel and is fully modulated by the resistance change of the interface between electrode and PCMO layer or between two oxide layers with different stoichiometry during resistive switching. However, resistance modulation mechanism helps with energy consumption is not helpful to the spike timing. Due to the slow redox reaction at the interface, the median of spike timing is up to milliseconds, as compared to the µs level timing of non-chemically reactive synaptic devices. On the other hand, interface-controlled devices are much more capable for the continuous signal with small dynamic range and the low fresh rate thanks to its low standby power and action energy, gifted from the oxygen interchange between the two layers, which modulates the interface conduction barrier only [104, 107, 125, 218]. Therefore, with the low standby power and moderate action energy among the classes, ICM is recommended for DNN accelerator applications, where requires rare updating and frequent reading, referring to Fig. 11b.

On the energy budget perspective, most benchmarked FTJ synaptic devices outperform the rest of the devices, shown in Fig. 11c. And one excellent HZO FTJ device [207] stands even out at 10 femtojoule per spike thanks to its ultra-thin switching layer (3.5 nm) with metallic oxide electrode (WO_x) which helps with a much lower barrier and also contributes for ohmic conduction, allowing enwidened hardware VMM application range. And thanks to its all plasma-enhanced atomic layered deposition (PE-ALD) fabrication process, the device obtains 10 billion write-erase cycles endurance. As suggested in Fig. 11b, FTJ devices are potential candidate for in-memory computing applications discussed in the opening sections, for their fast spike timing and low action energy that can be adapted for frequent and fast updating of the synaptic weight requirement. As an emerging device, mem-capacitor device consumes low standby power and moderate action energy shown in Fig. 11a. As a promising candidate as it is, however, due to the limited reports on this kind of device, further analysis and comparison is not possible to date. More investigation is encouraged to enrich the research in this area.

B. Benchmark for Artificial Neuron

Benchmark for artificial neuron is provided in Fig. 11c. Unlike the artificial synapse application, a stand-alone device can emulate. Most artificial neuron has an external circuitry, accompanied by a source resistor, parallel capacitor for charging and discharging during refractory period, and a load

This journal is © The Royal Society of Chemistry 20xx

Please do not adjust margins

Please do not adjust margins

resistor. Some even equipped with amplifier. It is not fair to compare device connected only to a load resistor with device equipped with a complex circuit with external power supply (for amplifier), even if some reports argued their stand-alone device is power efficient. Therefore, to ensure the fairness, benchmarking here refers to the net power consumption used in the neuron system, not just the device itself, as defined by the spiking energy and firing energy in the eq. 3 and eq. 4, respectively.

$$E_s = V_{spike}^2 \times G_{off} \times \tau_{spike} \text{ (eq. 3)}$$

$$E_f = V_{spike}^2 \times G_{on} \times \tau_{spike} \text{ (eq. 4)}$$

where E_s and E_f are the spiking and firing energy in Joule, respectively. Same as the artificial synapse devices, V_{spike}, G_{on}, G_{off} , and τ_{spike} are input spike voltage in Volt, LRS conductance in Siemens, HRS conductance in Siemens, and spike timing (pulse duration) in Second, respectively.

Spiking energy

The operation of artificial LIF or IF neuron device relies on the input spike trains, which means only a single spike will have minor impact on firing, especially for LIF neuron devices. However, a continuous spike train is required to fire the device, which consumes the most power if device requires many spikes to fire. Thus, the benchmarking of artificial neuron devices shall consider the energy consumption of spikes inputs towards the neuron even at refractory period, where the firing has not yet or just happened. And the spiking energy characterizes the energy consumption per spike during this period. Note that if there exists a source resistor R_s in the neuron circuit, it will substitute the device at HRS ($G_{off} = 1/R_s$).

Firing energy

It is adopted to characterize the energy consumption per spike when the neuron is fired. In the most benchmarked device, firing energy is within the order as spiking energy, but some devices possess much lower LRS which results in the high firing energy that is not negligible for the applications, which is the reason firing energy is separately benchmarked.

Discussion

As the number of reports focusing on artificial neuron by memristive devices is limited, this review may not be able to provide an overall inter-device comparison of memristive neurons. However, based on the data availability, Fig. 11c summarized the energy benchmarking of memristive neurons. The majority is ECM devices, as we have mentioned earlier, that due to the easy transition between non-volatile and volatile switching of most ECM devices by using compliance current, they can emulate the tuneable (leaky) integrate-and-firing functions with ease. High firing energy consumption, however, is accompanied with the ECM devices, with an exception by Bousoulas *et al.*[233] who managed and hypothesised to barrier Ag migration using $SiO_2/SiO_{2.07}$ bilayer structure and to form thin filament by using rough bottom electrode enabled by Pt NPs.

Besides of ECM neurons, some used ICM devices [242], PCM devices [173, 243], Si Nanorod [232], mixed-ionic conduction device [239], and van der Waals heterojunction device [238]. It is rather worth to mention that instead of avoiding the discussion of stochasticity of artificial neurons, Tuma *et al.* exploit the stochasticity nature of PCM neuron devices [173]. Cycle-to-cycle variability is found to be normal distributed of the inter-spike intervals, owing to which issue, they introduced population code using the number of neuron devices to compensate the neuron stochasticity, especially when input spikes are at high-frequency, and therefore, increase the system robustness. Besides, their neurons consume low firing and spiking energy because of the well-investigated spike timing-interval dependencies, enlightening a possible path to overcome the energy consumption issue to the most artificial neurons.

6. Challenge, Guideline, and Outlook

As a revolutionary and promising technology as neuromorphic device and computing are, the imagination of the future for neuromorphic is still in its infancy. However, lots of efforts have been made to pave the road of it by many researchers in every possible direction. In 2022, a roadmap on neuromorphic computing and engineering was proposed by leading scientists in their fields to discuss the insightful perspectives, where the engaged audiences may refer to for more future envisions. Here, based on our benchmarking data, we conclude some useful insights on device level challenges, design guidelines, and outlooks [245].

A. Challenge

Although many papers reported artificial synapses and neurons made of resistive switching-based emerging devices in the last decade, ANN performance was usually illustrated through simulation based on device measurement data. There have been several reports on array-level work [70, 147, 246], but none matched the performance of current GPU-based systems. The first system-level implementation with performance exceeding that of the GPU counterpart was made by Yao *et al.* [68] in early 2020. The delay in device to array implementation may be ascribed to two major challenges.

The first is variability, Fig. 12 shows the statistics of variation problem, both device-to-device (inter-device variation) and cycle-to-cycle (intra-device variation) for a given device structure. This problem is particularly severe in memristors that depend on the formation and rupture of a conducting filament as the basis for resistance switching. For example, Mahadevaiah *et al.* [110] reported the current variation in a 64 by 64 packed VCM array after forming, where the variation is random overall and deterministic in certain region, which might be contaminated during fabrication [111]. They also explored the cumulative probability of devices' current after the 1st, 10th, and 100th set and reset pulses over 100 devices, showing a wide and stochastic distribution of the pulse (A.C.) operation [111].Such a problem can be caused by intrinsic properties of the switching material. As shown in Fig. 12 a-c, by changing the switching material, the distribution of LRS and HRS current are improved over cycles and among 1,000 devices [172]. The stochastic nature of filament formation and rupture, exacerbated by

This journal is © The Royal Society of Chemistry 20xx

Please do not adjust margins

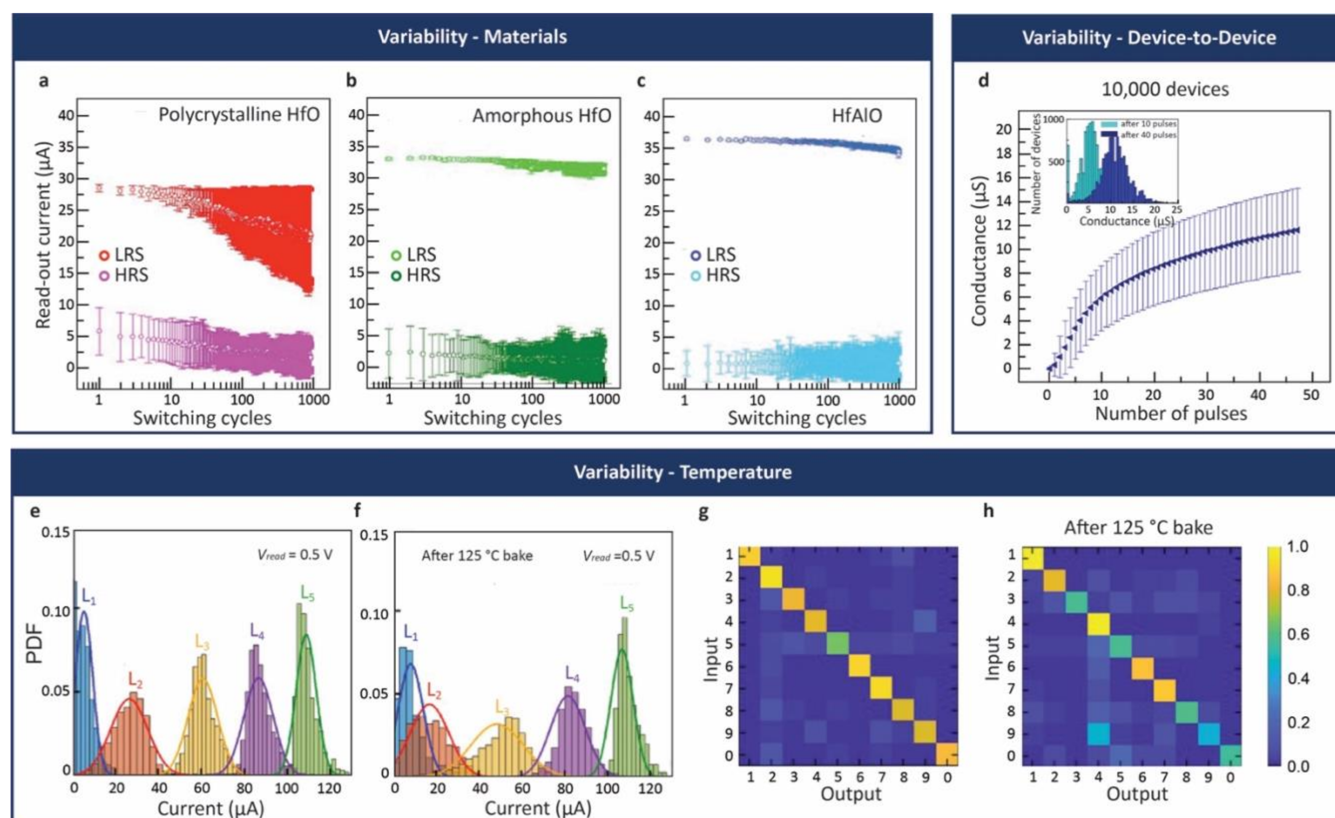

Fig. 12 Challenges on variability. a-c, Variability caused by materials on device-to-device over cycles statistics: pulse (A.C.) endurance test for 1,000 devices with different switching materials, i.e., pHfO for polycrystalline hafnia (**a**), aHfO for amorphous hafnia (**b**), and HfAlO for hafnium aluminium oxide (**c**) ($|V_{set}|$=1.2 V, $|V_{reset}|$=1.8 V). **d**, Device-to-device variation on over 10^4 PCM cells with 50 consecutive potentiation pulses (t_{pulse} = 50 ns, I_{pulse} = 100 µA) operation. The inset of **b** shows device conductance distribution after 10 and 40 pulses, shapes both normal distributions. **e-h**, Temperature instability for multibit operation: **e and f**, current probabilistic density function read at 0.5 V before (**e**) and after (**f**) 125 Celsius degree bake, where the latter shows a significant overlap between current states between the states. **g-h**, Confusion matrix on MNIST classification results before (**g**) and after (**h**) 1 hour annealing, accuracy drops from 86.5% to 72% after 125 Celsius degree baking. **Credits**: **a-c** and **g-h** are reproduced under CC-BY licence from ref. [111], copyright Milo *et al.* 2019 AIP Publishing; **d** is reproduced under CC-BY licence from ref. [172], copyright Sebastian *et al.* 2017 Springer Nature.

manufacturing induced jitters, has caused significant variation of programmed resistance values used to represent the weights in the ANN. Random variations in weights have been shown to negatively impact network's learning and prediction accuracy [111, 171, 172, 247]. Because with the intra-device variation, the resistance can sometimes overlap with each other, causing inaccurate weight storage. This is worsened by the superposition effect of the inter-device variation for the array level application, as shown in Fig. 12 d. As shown in Fig. 12 e and f, for a 5-level storage device, the probabilistic density function (PDF) of the current overlaps after temperature retention, which causes the disturbance in training and testing of a two-layer neural network, dropping from 82.6% accuracy to 72% on MNIST database[172]. As compared to the results from fresh sample showed in Fig. 12 g, the confusion matrix of the testing result in Fig. 12 h clearly shows the compromised results. The problem also renders online network training impractical. Training is carried out offline via simulation and then the optimized weights programmed into the memristor array. On the other hand, the issue is less severe in interface-controlled memristor devices because of the better resistance modulation in a small dynamic range, as analysed in the benchmark. For instance, Yao *et al.* [68] used ICM device and discussed in its physics that devices' resistance states are only modulated between the interfacial layers given good control and stability, and therefore suitable for hybrid training (baseline weights obtained offline and updating online) CNN accelerator and achieved 3.81% final test error on MNIST dataset.

The other challenge lies in the sneak path current in a passive crossbar array and the lack of a compact, reliable selector or access device to suppress it. A sneak path current is a parasitic current added, by neighbouring memristors in the low-resistance state, to the read current of a memristor in the high-resistance state thus giving rise to a wrong read-out value. The typical way to solve this problem is to isolate memristors from one another using access transistors [169], like in the current dynamic random-access memory. However, doing so erodes the high integration density and process simplicity advantages of the crossbar architecture. Some researchers have proposed threshold or volatile switching devices having the same structure as memristors as potential selector devices [214, 248]. The sneak path current issue has on the other hand motivated the development of memory transistors which combine both the select and memory functions in a single device.

Another issue with memristor lies with the implementation of the STDP learning rule, which is crucial to the operation of SNN. As shown in many papers [140, 249], shaping and overlapping of voltage waveforms at the two terminals are required to achieve the desired outcomes. This adds substantial complexity to the design of supporting circuitry. To date, system-level

Please do not adjust margins
Please do not adjust margins

implementation of SNN based on memristors has not been demonstrated.

B. Guideline

From the proposed benchmark and the analysis of a tiny corner of the publications, we screen out several pathways on low-energy consumption, high-speed, and high-robustness artificial neuron and synapse devices towards the neuromorphic electronics era. Here, useful insights on the statistical data regarding the memristive devices are introduced.

Intra-Device Design

As discussed earlier, there is never a perfect device, but always room for perfection. Summarized from the benchmark, three pathways to optimize the filamentary type devices for synaptic applications are illustrated in Fig. 13. The rule of thumb in filamentary neuromorphic devices is the engineering of the filaments. The most intuitive but aggressive way is confining the conductive filament by direct etching of the dielectrics, gives a physical channel for the flow of filament, as illustrated in Fig. 13a [147]. The confined filaments contribute on a mostly linear potentiation and depression (Fig. 13b), as well as low device-to-device and die-to-die variation. Less aggressively, the filament can be controlled precisely with electro-manipulation. Rao et al. used a customed write-verification programming method to achieve nanoscale filament control shown in Fig. 13c, where small pulses with precise control reduces the filament sizes confirmed in the C-AFM images. And eventually, it gives 2,048 conductance states shown in Fig. 13d.

Another major optimization path is to reduce the filament by material designing. Here two designs of memristive neuromorphic devices with common feature are stressed: conduction engineering (Fig. 13e and f) and electron/thermal (barrier) modulation and filament (Fig. 13h and i). Firstly, from Fig. 11a, the energy consumption per spike for different devices spreads from tens of femto-Joules to hundreds of milli-Joules. It is obvious that Joule heat contributes most besides the energy used for switching since there are no light, sound, or haptic emission during switching. Thus, to control heat generation is one of the most important ways to reduce energy consumption, especially action energy. One approach is to create potential barrier by introducing multiple layers to slow filament migration (Fig. 13e) [94, 101, 225] or using less diffusive filaments as the electrode [122, 244]. The benefit of multiple repeating layers reflected in the good linearity of potentiation and depression shown in Fig. 13g. Another design is to introduce a single modulation layer to mitigate the filament formation and rupture (Fig. 13h). Among materials used in the benchmarked devices, TaO_x [104, 107, 125, 218], TiO_x [115], and VO_x [214] are investigated and reported to have such functions. Shown in Fig. 13i, they function as the overshoot suppression layer by modulating the conductive filament diffusion, which is also a key factor to reduce the action energy, increase linearity of synapse potentiation and depression, and to lower the standby power. While Rao *et al.* 's work also adopted the similar approach using nanometre thin Al_2O_3 and Ti functioning as electro/thermal modulation layer to help with filament control.

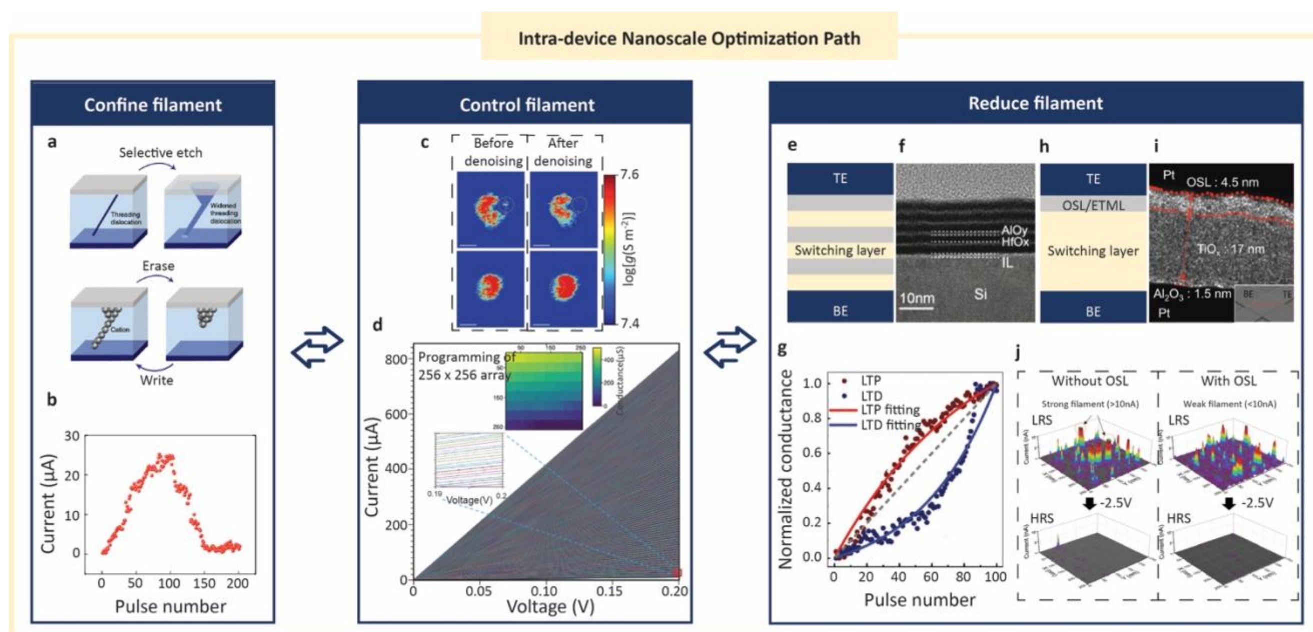

Fig. 13 Intra-device nanoscale optimization path for neuromorphic applications. **a**, Selective etch of epitaxial SiGe to form a channel for metal filaments. **b**, Long-term potentiation and depression of the epi-SiGe devices, showing good linearity. **c**, C-AFM image of $Ta/Ti/Al_2O_3/HfO_2/Pt$ device before and after using a custom denoising write-verification pulse program, showing a better control filament using such pulsing scheme. d, the 2,048 conductance states giving from fine conductance tuning of the device in **c**. **e**, device with multiple repeated switching layers, or superlattice-like (SLL) structure, TEM image of such structure shown in **f**. **g**, Enhanced long-term potentiation and depression achieved by SLL device in **f**. **h**, device with device with overshoot suppression layer (OSL) or electro-/thermal modulation layer (ETML), TEM image of such structure shown in **i**. **j**, C-AFM image comparison of the device without OSL and with OSL in LRS and HRS, confirming the reduced filament size in OSL devices. **Credits**: **a-b** are reproduced with permissions from ref. [147], copyright 2018 Choi *et al.* 2017, under exclusive licence to Macmillan Publishers Limited, part of Springer Nature; **c-d** are reproduced with permission from ref.[212], copyright 2023 Rao *et al.* under exclusive licence to Springer Nature Limited; **e** is adapted from ref. [104, 107, 115, 125, 214, 218]; **f and g** is reproduced under CC-BY licence from ref. [101], copyright Wang *et al.* 2022 Wiley-VCH GmbH; **h** is adapted from ref. [94, 101, 225]; **i and j** are reproduced under CC-BY licence from ref. [115], copyright Kim *et al.* 2022 Wiley-VCH GmbH.

On the complete contrary, non-filament switching layer are used to suppress the conduction of electron/vacancies and heat [149, 150, 153, 154]. Good energy control of ferroelectric and spintronic devices can also be attributed to the same reason, that switching is modulated by using potential difference of electron dipole and different orbit of magnetization, allowing no actual filament conduction inside the device, which ultimately results for little Joule heat generation.

Inter-Device Configuration

Until now, focuses are kept on device level discussion (intra-device). It is not enough, however, without mentioning the device-to-device configuration (inter-device). Typically, intra-device stacks are simple: metal-insulator-metal (MIM) for most devices and metal-ferroelectric-insulator-semiconductor (MFIS) for ferroelectric devices. Shown in Fig. 14a-g, inter-device configurations are various enabled by the innovative ideas of people: passive crossbars shown in Fig. 14a (1 memristive device only, 1MR crossbar), active crossbars Fig. 14b (1 memristive device built on the drain of transistor, 1T1MR crossbar, or 1 selector built on the top of the memristive device [248], 1S1MR, or 1 memristive device connect to the source of the ferroelectric transistor [250], 1F1MR), 2 series memristive devices/crossbars shown in Fig. 14c (series connection of 2 memristive devices [142], series-2MR, or reconfigurable selector/memristor enabled by two switching layers [214], 1S/MR).

Active and passive crossbars

As shown in Fig. 14a-b, crossbar (cross-point, x-bar) configuration comprises the device(s) connected by two

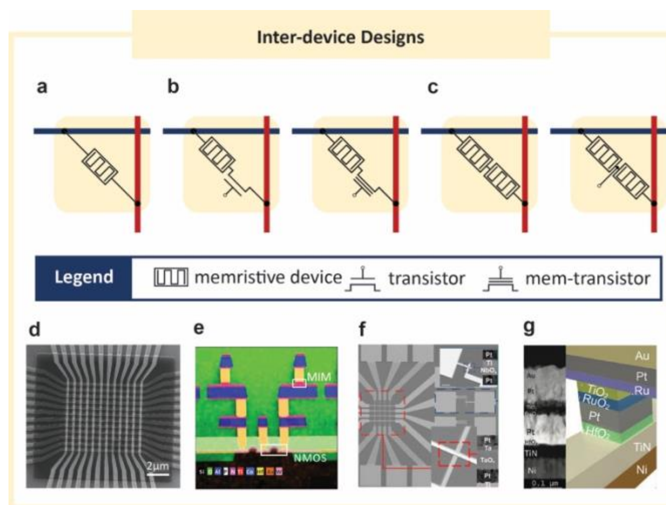

Fig. 14 Inter-device designs: **a**, passive crossbar structure (SEM image of a 10 by 10 memristor array is shown in **d**). **b**, active crossbar structure, the pass transistor or selector offers the third terminal to these configurations, where the pass transistor or selector could be traditional field effect transistor whose SEM-EDX image is shown in **e**, or ferroelectric field effect transistor. **c**, series memristors, typically with (right) the inter-devices third terminal, which can be in planar structure and connected by interconnects (SEM shown in **f**, where the upper inset is the NbO_x memristor and the lower inset is the TaO_x memristor, with their respective TEM image) or vertically stacked (TEM image and schematic shown in **g**). **Credits**: **d** is reproduced with permission from ref. [69], copyright Prezioso *et al.* 2015 Springer Nature Limited, **e** is reproduced under CC-BY licence from ref. [111] copyright Milo *et al.* 2019 AIP Publishing; **f** is reproduced under CC-BY licence from ref. [142], copyright Duan *et al.* 2020 Springer Nature; and **g** is reproduced with permission from ref. [248], copyright Woo *et al.* 2022 Wiley-VCH GmbH.

perpendicular electrodes. No matter active or passive, crossbar connection makes large scale integration of memristive neuron or synapse devices possible and requires CMOS-compatible fabrication process, which brings more challenges on variation control in deposition, lithography, etching, etc., especially for emerging materials. No pain, no gain, nevertheless, the complex and high-standard fabrication trades off for more opportunities. Passive crossbars progress slowly since the first validation of passive crossbar idea by Prezioso *et al.* on a 10 by 10 array (Fig. 14d) [69] because of the sneak path challenges of passive crossbar, as elaborated in the above sections. In our benchmark, standby power metrics show the potential of a device to minimize sneak path current. Particularly, standby power of FTJ and interfaced-controlled memristive devices is significantly lower than the others shown in Fig. 11c, which promotes their potential in passive array application: The 5 by 5 FTJ array built by Berdan *et al.* showed that the VMM error of the output expectation is normal distributed with standard deviation of 0.77% (6-bit analogue precision), and the estimated power consumption of which under F-MNIST network gives a 157.5 TOPS/W efficiency [70].

On the active crossbars shown as Fig. 14e, substantial progress has been made with the help of the most advanced fabrication foundry since the first demonstration of a PCM active array [251]. In 2021, Xue *et al.* achieved 195.7 TOPS/W edge computation by a 4-megabits 8-precision ReRAM chip built with 22 nm technology [252], which evolved from 14.6 ns MAC speed (53.17 TOPS/W) by a 1 megabits 8-precision ReRAM chip based on 55 nm technology [253]. Among active crossbar configurations, 1F1MR and 1S1MR are the most unique. Chen *et al.* built a 4-bit 1F1MR crossbar array, a memristive device with connection to the source of one ferroelectric transistor which provides more memory states than the single-state access transistor[250] .

Series devices (crossbars)

Duan *et al.* introduced a 4 by 4 passive array of non-volatile memristive synaptic devices in series connection with volatile neuron device [142], shown in Fig. 14f, emulating 8 neurons fully connected by 16 synapses, based on which they demonstrated supervised pattern recognition and coincide detection. Woo *et al.* built a three-terminal device with one selector device stacked on the top of memristive device with a middle selector electrode to minimize the sneak path current as shown in Fig. 14g [248]. This compact device array can perform 3 by 3 bit “L”, “I”, and “X” pattern classification accurately using pre-trained synaptic weight.

C. Outlooks

Spatial-temporal signal processing by memristive neuron and synapses

Spatial signal detection with memristive devices can be traced back as early as 2012, Kuzum *et al.* using simulation based on PCM devices performed the distorted letter reconstruction and noise reduction [164] and Kim *et al.* using a 40 by 40 active ECM array to reconstruct the input bitmap logo as shown in Fig. 15a where the corresponding device conductance distribution remains the window (Fig. 15b) [136]. While their work centred on spatial signal reconstruction, Sabastian *et al.* [172] used 1 million

PCM array to map the temporal signals, where the temporal rainfall data were feed to the array by several series of pulse trains in Fig. 15c and the conductance states of device array showed good correspondence to the inputs in Fig. 15d.

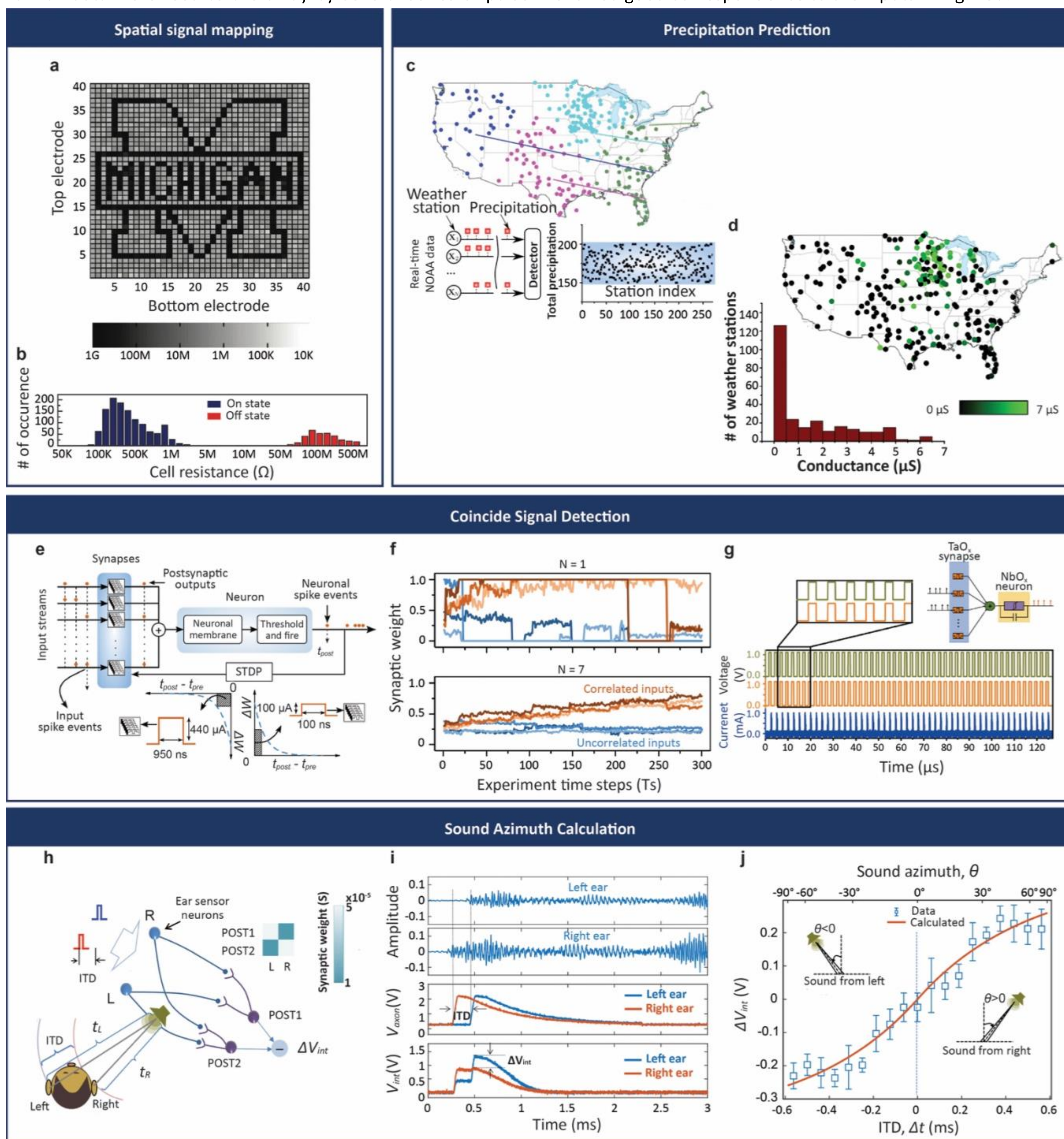

Fig. 15 Spatial-temporal signal processing by memristive devices. a and **b**, spatial signal mapping using 40 by 40 active ECM array where a is the reconstructed bitmap image and b is the distribution of 1,600 device conductance states showing no overlapping between states. **c** and **d**, temporal signal mapping using 1000 by 1000 PCM device array to map the real rainfall data in a time-series pulse train(**c**) to the device array where it shows excellent correlation between the rainfall precipitance and the device conductance(**d**). **e** and **f**, spatial-temporal signal classification using 1000 synapses x N PCM devices per synapse and one software LIF neuron based on STDP learning rule (**e**), in which the correlated inputs can be well distinctive from the others when N = 7 (**f**). **g**, spatial-temporal signal classification using multi- TaO_x synapses and NbO_x LIF neuron (inset of **g**) to detect the input correlation or synchronous input pulses, where synchronized events are the output current in blue colour. **h**-**j**, Sound azimuth angle detection by a 2 by 2 synapse array (**h**). The inputs of left and right ear (upper waveform in **i**) different by an inter-aural time difference (ITD, middle waveform in **i**) gives a differential V_{int} (lower waveform in **i**) which can be fitted to the red curve in **j** to identify the sound azimuth angle. **Credits**: **a** and **b** are reprinted with permission from ref. [136], copyright Kim *et al.* 2012 American Chemical Society; **c** and **d** are reproduced under CC-BY licence from ref. [172], copyright Sebastian *et al.* 2017 Springer Nature; **e** and **f** are reproduced under CC-BY licence from ref. [171], copyright Boybat *et al.* 2018 Springer Nature; **g** is reproduced under CC-BY licence from ref. [142], copyright Duan *et al.* 2020 Springer Nature; **h**-**j** are adapted under CC-BY-NC licence from ref. [85], copyright Wang *et al.* 2018 AAAS.

Please do not adjust margins

Spatial-temporal signal processing, or simplified hardware SNN is realized later using 1,000 synapses with N-PCM devices each synapse by Boybat *et al.* [171] to a software LIF neuron shown in Fig. 15e. Experimental results in Fig. 15f show the 7-PCM synapse with 1 software neuron can distinguish the correlated inputs by STDP learning rule. To make the fully memristive SNN, Duan *et al.* [142] use TiO_x synapse and NbO_x LIF neuron to emulate the biological neural network. The schematic is shown in the inset of Fig. 15g and SEM and TEM of device array and cross-section of single device are shown in Fig. 14f. Their system can detect the coincide signal (green and orange waveform) and spikes through the NbO_x artificial neuron as shown in blue waveform in Fig. 15g. Wang *et al.* [85] then developed a sound azimuth angle detection system using 2 by 2 synapses array based on STDP learning rule, as shown in Fig. 15h. As elaborated in Fig. 15i, the sound wave travels different distance before reaching left and right ears, so the inter-aural time difference (ITD) between two inputs will pass to the synapses where one synapse is inhibited and the other is excited because of STDP. In turn, a voltage difference taken between the two synapses could be correlated with ITD, which can be transposed into sound azimuth angle, as shown in Fig. 15j.

7. Summary

Amazed by the natural beauty of the neurons and synapses, researchers have re-invented the basic computing unit of the silicon-based chips and named it commonly as neuromorphic devices. Neuromorphic devices are hoped to be the driving force to overcome the bottlenecks we have created in the current IC technologies: power, speed, and communication of the processor, memory, and sensor. Fantasies or reality, neuromorphic devices gained enormous attentions, nevertheless. It is indeed the time to peel off the clothes of this new emperor and review the progress made so far in a fair criterion. Therefore, along the journey this article has led, the emergence of neuromorphic devices and advances with current technologies are briefed, nanoscale mechanisms of resistive-switching based neuromorphic devices are discussed, and mostly, universal benchmarks of the devices for synaptic applications are introduced, based on which the challenges are analysed, guidelines are suggested, and outlooks are envisioned. Reports on the neuromorphic devices were presented in such delicate ways with fantastic data and imaginative but practical applications that one may find it difficult to compare fairly. However, with the provided benchmark, this work enables the comparison of substantial metrics on energy and speed performance between various neuromorphic devices.

Thomas Edison did not invent light bulb in one night and he surely cannot envision a world with countless light-emitting diodes in their pockets. However, he taught the story of believing in the failures. Here, by committing to the drawbacks found by analysing the reported works, possible guidelines for intra-device and inter-device optimization on the resistive-switching based devices are recommended. The outlooks on the applications of neuromorphic devices are discussed briefly to show the capability of them. And admittedly, in this emerging field, the only limitation is the imagination. Combining all the power and creativity the neuromorphic devices carried with, we may foresee the brain on a chip in the near future.

Conflicts of interest

There are no conflicts to declare.

Acknowledgements

This work was supported by the Singapore Ministry of Education under Research Grant MOE-T2EP50120-0003.

References

1. W. S. McCulloch and W. Pitts, *The Bulletin of Mathematical Biophysics*, 1943, **5**, 115-133.
2. F. Rosenblatt, *The Perceptron — A Perceiving and Recognizing Automaton*, Cornell Aeronautical Laboratory, Inc., New York, 1957.
3. Y. LeCun, Y. Bengio and G. Hinton, *Nature*, 2015, **521**, 436-444.
4. A. G. Ivakhnenko, *Soviet Automatic Control*, 1968, **1**, 12.
5. P. J. Werbos, in *System Modeling and Optimization*, Springer-Verlag, 1982, DOI: 10.1007/BFb0006203, ch. Chapter 84, pp. 762-770.
6. A. G. Ivakhnenko, *IEEE Transactions on Systems, Man, and Cybernetics*, 1971, **SMC-1**, 364-378.
7. S. Linnainmaa, Master's Thesis, Univ. Helsinki, 1970.
8. Y. LeCun, B. Boser, J. S. Denker, D. Henderson, R. E. Howard, W. Hubbard and L. D. Jackel, *Neural Computation*, 1989, **1**, 541-551.
9. M. Minsky and S. Papert, *Perceptrons, reissue of the 1988 expanded edition with a new foreword by Léon Bottou: an introduction to computational geometry*, MIT press, 2017.
10. C. M. Berners-Lee, *Nature*, 1968, **219**, 202-203.
11. G. Hinton, S. Osindero, M. Welling and Y. W. Teh, *Cognitive Science*, 2006, **30**, 725-731.
12. M. A. Ranzato, C. Poultney, S. Chopra and Y. LeCun, Proceedings of the 19th International Conference on Neural Information Processing Systems, Canada, 2006.
13. Q. V. Le, 2013 IEEE International Conference on Acoustics, Speech and Signal Processing, Vancouver, BC, Canada, 2013.
14. D. Ciresan, U. Meier and J. Schmidhuber, 2012 IEEE Conference on Computer Vision and Pattern Recognition, Providence, RI, USA, 2012.
15. W. Maass, Advances in Neural Information Processing Systems 7 (NIPS 1994), Denver, Colorado, USA, 1995.
16. W. Maass, *Neural Computation*, 1996, **8**, 1-40.
17. W. Maass, *Neural Networks*, 1997, **10**, 1659-1671.
18. K. Roy, A. Jaiswal and P. Panda, *Nature*, 2019, **575**, 607-617.
19. L. Jim-Shih and T. W. Berger, Proceedings. IEEE World Congress on Computational Intelligence, Anchorage, AK, USA, 1998.
20. C. Näger, J. Storck and G. Deco, *Neurocomputing*, 2002, **44-46**, 937-942.
21. C. Panchev and S. Wermter, *Neurocomputing*, 2004, **58-60**, 365-371.
22. S. Loiselle, J. Rouat, D. Pressnitzer and S. Thorpe, Proceedings. 2005 IEEE International Joint Conference on Neural Networks, 2005, Montreal, QC, Canada, 2005.

This journal is © The Royal Society of Chemistry 20xx

Please do not adjust margins

Please do not adjust margins

23. A. Gupta and L. N. Long, 2007 International Joint Conference on Neural Networks, Orlando, FL, USA, 2007.
24. M.-J. Escobar, G. S. Masson, T. Vieville and P. Kornprobst, *International Journal of Computer Vision*, 2009, **82**, 284-301.
25. B. J. Kröger, J. Kannampuzha and C. Neuschaefer-Rube, *Speech Communication*, 2009, **51**, 793-809.
26. B. Meftah, O. Lezoray and A. Benyettou, *Neural Processing Letters*, 2010, **32**, 131-146.
27. J. J. Wade, L. J. McDaid, J. A. Santos and H. M. Sayers, *EEE Transactions on Neural Networks and Learning Systems*, 2010, **21**, 1817-1830.
28. S. G. Wysoski, L. Benuskova and N. Kasabov, *Neural Networks*, 2010, **23**, 819-835.
29. A. Tavanaei and A. Maida, Neural Information Processing: 24th International Conference, Guangzhou, China, 2017.
30. D. Hassabis, D. Kumaran, C. Summerfield and M. Botvinick, *Neuron*, 2017, **95**, 245-258.
31. R. Miikkulainen, J. Liang, E. Meyerson, A. Rawal, D. Fink, O. Francon, B. Raju, H. Shahrzad, A. Navruzyan, N. Duffy and B. Hodjat, in *Artificial Intelligence in the Age of Neural Networks and Brain Computing*, eds. R. Kozma, C. Alippi, Y. Choe and F. C. Morabito, Academic Press, 2019, pp. 293-312.
32. R. Girshick, Proceedings of the IEEE International Conference on Computer Vision (ICCV), Santiago, Chile, 2015.
33. P. A. Merolla, J. V. Arthur, R. Alvarez-Icaza, A. S. Cassidy, J. Sawada, F. Akopyan, B. L. Jackson, N. Imam, C. Guo, Y. Nakamura, B. Brezzo, I. Vo, S. K. Esser, R. Appuswamy, B. Taba, A. Amir, M. D. Flickner, W. P. Risk, R. Manohar and D. S. Modha, *Science*, 2014, **345**, 668-673.
34. C. Sung, H. Hwang and I. K. Yoo, *Journal of Applied Physics*, 2018, **124**, 151903.
35. C. S. Thakur, J. L. Molin, G. Cauwenberghs, G. Indiveri, K. Kumar, N. Qiao, J. Schemmel, R. Wang, E. Chicca, J. Olson Hasler, J. S. Seo, S. Yu, Y. Cao, A. van Schaik and R. Etienne-Cummings, *Front NeurosciFrontiers in Neuroscience*, 2018, **12**, 891.
36. D. Marković, A. Mizrahi, D. Querlioz and J. Grollier, *Nature Reviews Physics*, 2020, **2**, 499-510.
37. Z. Wang, H. Wu, G. W. Burr, C. S. Hwang, K. L. Wang, Q. Xia and J. J. Yang, *Nature Reviews Materials*, 2020, **5**, 173-195.
38. W. Zhang, B. Gao, J. Tang, P. Yao, S. Yu, M.-F. Chang, H.-J. Yoo, H. Qian and H. Wu, *Nature Electronics*, 2020, **3**, 371-382.
39. R. Yuste, *Nature Reviews Neuroscience*, 2015, **16**, 487-497.
40. E. R. Kandel, S. Mack, T. M. Jessell, J. H. Schwartz, S. A. Siegelbaum and A. J. Hudspeth, McGraw-Hill Medical, New York, NY, 5th edn., 2014, pp. 67-330.
41. A. L. Hodgkin and A. F. Huxley, *The Journal of Physiology*, 1952, **117**, 500-544.
42. N. Brunel and M. C. W. van Rossum, *Biological Cybernetics*, 2007, **97**, 341-349.
43. B. Gluss, *The bulletin of mathematical biophysics*, 1967, **29**, 233-243.
44. B. K. Roy and D. R. Smith, *The bulletin of mathematical biophysics*, 1969, **31**, 341-357.
45. C. D. Geisler and J. M. Goldberg, *Biophysical Journal*, 1966, **6**, 53-69.
46. C. Pozzorini, R. Naud, S. Mensi and W. Gerstner, *Nature Neuroscience*, 2013, **16**, 942-948.
47. R. Naud, N. Marcille, C. Clopath and W. Gerstner, *Biological Cybernetics*, 2008, **99**, 335-347.
48. R. Jolivet, A. Rauch, H.-R. Lüscher and W. Gerstner, *Journal of Computational Neuroscience*, 2006, **21**, 35-49.
49. A. N. Burkitt, *Biological Cybernetics*, 2006, **95**, 1-19.
50. T. H. Murphy and D. Corbett, *Nature Reviews Neuroscience*, 2009, **10**, 861-872.
51. R. Menzel, *Nature Reviews Neuroscience*, 2012, **13**, 758-768.
52. Y.-S. Lee and A. J. Silva, *Nature Reviews Neuroscience*, 2009, **10**, 126-140.
53. M. J. Rozenberg, O. Schneegans and P. Stoliar, *Scientific Reports*, 2019, **9**, 11123.
54. S. G. Hormuzdi, M. A. Filippov, G. Mitropoulou, H. Monyer and R. Bruzzone, *Biochimica et Biophysica Acta (BBA) - Biomembranes*, 2004, **1662**, 113-137.
55. D. Purves, G. J. Augustine, D. Fitzpatrick, W. C. Hall, A.-S. LaMantia, J. O. McNamara and L. E. White, in *Neuroscience*, Sinauer Associates, Sunderland, MA, US, 4th edn., 2008, pp. 85-88.
56. D. O. Hebb, *The organization of behavior; a neuropsychological theory*, Wiley, Oxford, England, 1949.
57. M. Taylor, *South African Journal of Psychology*, 1973, **3**, 23-45.
58. W. B. Levy and O. Steward, *Neuroscience*, 1983, **8**, 791-797.
59. Y. Dan and M. M. Poo, *Science*, 1992, **256**, 1570-1573.
60. D. Debanne, B. H. Gahwiler and S. M. Thompson, *Proceedings of the National Academy of Sciences of the United States of America*, 1994, **91**, 1148-1152.
61. H. Markram, J. Lubke, M. Frotscher and B. Sakmann, *Science*, 1997, **275**, 213-215.
62. G. Q. Bi and M. M. Poo, *Journal of Neuroscience*, 1998, **18**, 10464-10472.
63. L. F. Abbott and S. B. Nelson, *Nature Neuroscience*, 2000, **3**, 1178-1183.
64. C. Koch and I. Segev, *Nature Neuroscience*, 2000, **3**, 1171-1177.
65. A. Destexhe and E. Marder, *Nature*, 2004, **431**, 789-795.
66. M. Hübener and T. Bonhoeffer, *Cell*, 2014, **159**, 727-737.
67. J. Pei, L. Deng, S. Song, M. Zhao, Y. Zhang, S. Wu, G. Wang, Z. Zou, Z. Wu, W. He, F. Chen, N. Deng, S. Wu, Y. Wang, Y. Wu, Z. Yang, C. Ma, G. Li, W. Han, H. Li, H. Wu, R. Zhao, Y. Xie and L. Shi, *Nature*, 2019, **572**, 106-111.
68. P. Yao, H. Wu, B. Gao, J. Tang, Q. Zhang, W. Zhang, J. J. Yang and H. Qian, *Nature*, 2020, **577**, 641-646.
69. M. Prezioso, F. Merrikh-Bayat, B. D. Hoskins, G. C. Adam, K. K. Likharev and D. B. Strukov, *Nature*, 2015, **521**, 61-64.
70. R. Berdan, T. Marukame, K. Ota, M. Yamaguchi, M. Saitoh, S. Fujii, J. Deguchi and Y. Nishi, *Nature Electronics*, 2020, **3**, 259-266.
71. B. Tang, H. Veluri, Y. Li, Z. G. Yu, M. Waqar, J. F. Leong, M. Sivan, E. Zamburg, Y.-W. Zhang, J. Wang and A. V.-Y. Thean, *Nature Communications*, 2022, **13**, 3037.
72. SONY, The world's first Intelligent Vision Sensor with edge processing, developer.sony.com/develop/imx500/, (accessed 10 Jul 2023).
73. C. Li, M. Hu, Y. Li, H. Jiang, N. Ge, E. Montgomery, J. Zhang, W. Song, N. Dávila, C. E. Graves, Z. Li, J. P. Strachan, P. Lin, Z. Wang, M. Barnell, Q. Wu, R. S. Williams, J. J. Yang and Q. Xia, *Nature Electronics*, 2018, **1**, 52-59.
74. M. A. Zidan, Y. Jeong, J. Lee, B. Chen, S. Huang, M. J. Kushner and W. D. Lu, *Nature Electronics*, 2018, **1**, 411-420.
75. S. Oh, Y. Shi, J. Del Valle, P. Salev, Y. Lu, Z. Huang, Y. Kalcheim, I. K. Schuller and D. Kuzum, *Nature Nanotechnology*, 2021, **16**, 680-687.
76. H. Mujtaba, NVIDIA Volta GV100 12nm FinFET GPU Detailed – Tesla V100 Specifications Include 21 Billion Transistors, 5120 CUDA Cores, 16 GB HBM2 With 900 GB/s Bandwidth, wccftech.com/nvidia-volta-gv100-gpu-tesla-v100-architecture-specifications-deep-dive/, (accessed 10-07-2023).

This journal is © The Royal Society of Chemistry 20xx

Please do not adjust margins

Please do not adjust margins

77. M. Le Gallo, A. Sebastian, R. Mathis, M. Manica, H. Giefers, T. Tuma, C. Bekas, A. Curioni and E. Eleftheriou, *Nature Electronics*, 2018, **1**, 246-253.
78. P. M. Sheridan, F. Cai, C. Du, W. Ma, Z. Zhang and W. D. Lu, *Nature Nanotechnology*, 2017, **12**, 784-789.
79. X. Guo, F. M. Bayat, M. Bavandpour, M. Klachko, M. R. Mahmoodi, M. Prezioso, K. K. Likharev and D. B. Strukov, 2017 IEEE International Electron Devices Meeting (IEDM), San Francisco, CA, USA, 2017.
80. S. Yu, Z. Li, P.-Y. Chen, H. Wu, B. Gao, D. Wang, W. Wu and H. Qian, 2016 IEEE International Electron Devices Meeting (IEDM), San Francisco, CA, USA, 2016.
81. G. W. Burr, R. M. Shelby, C. Di Nolfo, J. W. Jang, R. S. Shenoy, P. Narayanan, K. Virwani, E. U. Giacometti, B. Kurdi and H. Hwang, 2014 IEEE International Electron Devices Meeting, San Francisco, CA, USA, 2014.
82. L. Chua, *IEEE Transactions on Circuit Theory*, 1971, **18**, 507-519.
83. D. B. Strukov, G. S. Snider, D. R. Stewart and R. S. Williams, *Nature*, 2008, **453**, 80-83.
84. L. O. Chua and S. M. Kang, *Proceedings of the IEEE*, 1976, **64**, 209-223.
85. W. Wang, G. Pedretti, V. Milo, R. Carboni, A. Calderoni, N. Ramaswamy, A. S. Spinelli and D. Ielmini, *Science Advances*, 2018, **4**, eaat4752.
86. D.-J. Seong, M. Hassan, H. Choi, J. Lee, J. Yoon, J.-B. Park, W. Lee, M.-S. Oh and H. Hwang, *IEEE Electron Device Letters*, 2009, **30**, 919-921.
87. H. S. P. Wong, S. Raoux, S. Kim, J. Liang, J. P. Reifenberg, B. Rajendran, M. Asheghi and K. E. Goodson, *Proceedings of the IEEE*, 2010, **98**, 2201-2227.
88. Y. F. Wang, Y. C. Lin, I. T. Wang, T. P. Lin and T. H. Hou, *Scientific Reports*, 2015, **5**, 10150.
89. N. Locatelli, V. Cros and J. Grollier, *Nature Materials*, 2014, **13**, 11-20.
90. A. Chanthbouala, R. Matsumoto, J. Grollier, V. Cros, A. Anane, A. Fert, A. V. Khvalkovskiy, K. A. Zvezdin, K. Nishimura, Y. Nagamine, H. Maehara, K. Tsunekawa, A. Fukushima and S. Yuasa, *Nature Physics*, 2011, **7**, 626-630.
91. V. Garcia and M. Bibes, *Nature Communications*, 2014, **5**, 4289.
92. G. Kim, S. Son, H. Song, J. B. Jeon, J. Lee, W. H. Cheong, S. Choi and K. M. Kim, *Advanced Science*, 2023, **10**, 2205654.
93. S. Ambrogio, S. Balatti, D. C. Gilmer and D. Ielmini, *IEEE Transactions on Electron Devices*, 2014, **61**, 2378-2386.
94. S. Yu, B. Gao, Z. Fang, H. Yu, J. Kang and H.-S. P. Wong, 2012 International Electron Devices Meeting, San Francisco, CA, USA, 2012.
95. K. V. Egorov, R. V. Kirtaev, Y. Y. Lebedinskii, A. M. Markeev, Y. A. Matveyev, O. M. Orlov, A. V. Zablotskiy and A. V. Zenkevich, *physica status solidi (a)*, 2015, **212**, 809-816.
96. Q. Wu, H. Wang, Q. Luo, W. Banerjee, J. Cao, X. Zhang, F. Wu, Q. Liu, L. Li and M. Liu, *Nanoscale*, 2018, **10**, 5875-5881.
97. C. Liu, L.-G. Wang, Y.-Q. Cao, M.-Z. Wu, Y.-D. Xia, D. Wu and A.-D. Li, *Journal of Physics D: Applied Physics*, 2020, **53**, 035302.
98. H. Zhang, X. Ju, K. S. Yew and D. S. Ang, *ACS Applied Materials & Interfaces*, 2020, **12**, 1036-1045.
99. O. G. Ossorio, G. Vinuesa, H. Garcia, B. Sahelices, S. Duenas, H. Castan, E. Perez, M. Kalishettyhalli Mahadevaiah and C. Wenger, *ECS Transactions*, 2021, **102**, 29-35.
100. C. Mahata, M. Ismail, M. Kang and S. Kim, *Nanoscale Research Letters*, 2022, **17**, 58.
101. C. Wang, G. Q. Mao, M. Huang, E. Huang, Z. Zhang, J. Yuan, W. Cheng, K. H. Xue, X. Wang and X. Miao, *Advanced Science*, 2022, **9**, 2201446.
102. Y. Matveyev, K. Egorov, A. Markeev and A. Zenkevich, *Journal of Applied Physics*, 2015, **117**, 044901.
103. Y. Matveyev, R. Kirtaev, A. Fetisova, S. Zakharchenko, D. Negrov and A. Zenkevich, *Nanoscale Research Letters*, 2016, **11**, 147.
104. P. Yao, H. Wu, B. Gao, S. B. Eryilmaz, X. Huang, W. Zhang, Q. Zhang, N. Deng, L. Shi, H.-S. P. Wong and H. Qian, *Nature Communications*, 2017, **8**, 15199.
105. J. Woo, K. Moon, J. Song, M. Kwak, J. Park and H. Hwang, *IEEE Transactions on Electron Devices*, 2016, **63**, 5064-5067.
106. J. Woo, K. Moon, J. Song, S. Lee, M. Kwak, J. Park and H. Hwang, *IEEE Electron Device Letters*, 2016, **37**, 994-997.
107. W. Wu, H. Wu, B. Gao, P. Yao, X. Zhang, X. Peng, S. Yu and H. Qian, 2018 IEEE Symposium on VLSI Technology, Honolulu, HI, USA, 2018.
108. E. Covi, S. Brivio, A. Serb, T. Prodromakis, M. Fanciulli and S. Spiga, 2016 IEEE International Symposium on Circuits and Systems (ISCAS), Montreal, QC, Canada, 2016.
109. G. González-Cordero, M. Pedro, J. Martin-Martinez, M. B. González, F. Jiménez-Molinos, F. Campabadal, N. Nafría and J. B. Roldán, *Solid-State Electronics*, 2019, **157**, 25-33.
110. M. K. Mahadevaiah, E. Perez, C. Wenger, A. Grossi, C. Zambelli, P. Olivo, F. Zahari, H. Kohlstedt and M. Ziegler, 2019 IEEE International Reliability Physics Symposium (IRPS), Monterey, CA, USA, 2019.
111. V. Milo, C. Zambelli, P. Olivo, E. Pérez, M. K. Mahadevaiah, O. G. Ossorio, C. Wenger and D. Ielmini, *APL Materials*, 2019, **7**, 081120.
112. C. Wenger, F. Zahari, M. K. Mahadevaiah, E. Perez, I. Beckers, H. Kohlstedt and M. Ziegler, *IEEE Electron Device Letters*, 2019, **40**, 639-642.
113. A. Wedig, M. Luebben, D. Y. Cho, M. Moors, K. Skaja, V. Rana, T. Hasegawa, K. K. Adepalli, B. Yildiz, R. Waser and I. Valov, *Nature Nanotechnology*, 2016, **11**, 67-74.
114. J. Woo, A. Padovani, K. Moon, M. Kwak, L. Larcher and H. Hwang, *IEEE Electron Device Letters*, 2017, **38**, 1220-1223.
115. S. Kim, J. Park, T.-H. Kim, K. Hong, Y. Hwang, B.-G. Park and H. Kim, *Advanced Intelligent Systems*, 2022, **4**, 2100273.
116. Y. Wu, S. Yu, H.-S. P. Wong, Y.-S. Chen, H.-Y. Lee, S.-M. Wang, P.-Y. Gu, F. Chen and M.-J. Tsai, 2012 4th IEEE International Memory Workshop, Milan, Italy, 2012.
117. S. G. Hu, Y. Liu, T. P. Chen, Z. Liu, Q. Yu, L. J. Deng, Y. Yin and S. Hosaka, *Applied Physics Letters*, 2013, **103**, 133701.
118. E. Yalon, A. A. Sharma, M. Skowronski, J. A. Bain, D. Ritter and I. V. Karpov, *IEEE Transactions on Electron Devices*, 2015, **62**, 2972-2977.
119. U. I. Bature, I. M. Nawi, M. H. M. Khir, F. Zahoor, S. S. Ba Hashwan, A. S. Algamili and H. Abbas, *Physica Scripta*, 2023, **98**, 035020.
120. R. Dittmann, S. Menzel and R. Waser, *Advances in Physics*, 2021, **70**, 155-349.
121. K. M. Kim, S. R. Lee, S. Kim, M. Chang and C. S. Hwang, *Advanced Functional Materials*, 2015, **25**, 1527-1534.
122. H. Jiang, L. Han, P. Lin, Z. Wang, M. H. Jang, Q. Wu, M. Barnell, J. J. Yang, H. L. Xin and Q. Xia, *Scientific Reports*, 2016, **6**, 28525.
123. L. Chen, Z.-Y. He, T.-Y. Wang, Y.-W. Dai, H. Zhu, Q.-Q. Sun and D. Zhang, *Electronics*, 2018, **7**, 80.
124. M. Ismail, U. Chand, C. Mahata, J. Nebhen and S. Kim, *Journal of Materials Science & Technology*, 2022, **96**, 94-102.

Please do not adjust margins

Please do not adjust margins

125. W. Wu, H. Wu, B. Gao, N. Deng, S. Yu and H. Qian, *IEEE Electron Device Letters*, 2017, **38**, 1019-1022.
126. J.-H. Ryu, C. Mahata and S. Kim, *Journal of Alloys and Compounds*, 2021, **850**, 156675.
127. X. Zhao, K. Zhang, K. Hu, Y. Zhang, Q. Zhou, Z. Wang, Y. She, Z. Zhang and F. Wang, *IEEE Transactions on Electron Devices*, 2021, **68**, 6100-6105.
128. Y. Zhang, G.-Q. Mao, X. Zhao, Y. Li, M. Zhang, Z. Wu, W. Wu, H. Sun, Y. Guo, L. Wang, X. Zhang, Q. Liu, H. Lv, K.-H. Xue, G. Xu, X. Miao, S. Long and M. Liu, *Nature Communications*, 2021, **12**, 7232.
129. C. Liaw, M. Kund, D. Schmitt-Landsiedel and I. Ruge, ESSDERC 2007 - 37th European Solid State Device Research Conference, Munich, Germany, 2007.
130. T. Hussain, H. Abbas, C. Youn, H. Lee, T. Boynazarov, B. Ku, Y. R. Jeon, H. Han, J. H. Lee, C. Choi and T. Choi, *Advanced Materials Technologies*, 2022, **7**, 2100744.
131. G. Dastgeer, H. Abbas, D. Y. Kim, J. Eom and C. Choi, *physica status solidi (RRL) – Rapid Research Letters*, 2021, **15**, 2000473.
132. M. Kund, G. Beitel, C. Pinnow, T. Rohr, J. Schumann, R. Symanczyk, K. Ufert and G. Muller, IEEE International Electron Devices Meeting, 2005. IEDM Technical Digest., Washington, DC, USA, 2005.
133. F. Zahoor, F. A. Hussin, U. B. Isyaku, S. Gupta, F. A. Khanday, A. Chattopadhyay and H. Abbas, *Discover Nano*, 2023, **18**, 36.
134. N. Lyapunov, X. D. Zheng, K. Yang, H. M. Liu, K. Zhou, S. H. Cai, T. L. Ho, C. H. Suen, M. Yang, J. Zhao, X. Zhou and J. Y. Dai, *Advanced Electronic Materials*, 2022, **8**, 2101235.
135. M. Suri, O. Bichler, D. Querlioz, G. Palma, E. Vianello, D. Vuillaume, C. Gamrat and B. DeSalvo, 2012 International Electron Devices Meeting, San Francisco, CA, USA, 2012.
136. K.-H. Kim, S. Gaba, D. Wheeler, J. M. Cruz-Albrecht, T. Hussain, N. Srinivasa and W. Lu, *Nano Letters*, 2012, **12**, 389-395.
137. Y. Yang, P. Gao, L. Li, X. Pan, S. Tappertzhofen, S. Choi, R. Waser, I. Valov and W. D. Lu, *Nature Communications*, 2014, **5**, 4232.
138. K. Krishnan, T. Tsuruoka, C. Mannequin and M. Aono, *Advanced Materials*, 2016, **28**, 640-648.
139. H. Abbas, A. Ali, J. Li, T. T. T. Tun and D. S. Ang, *IEEE Electron Device Letters*, 2023, **44**, 253-256.
140. H. Abbas, Y. Abbas, G. Hassan, A. S. Sokolov, Y.-R. Jeon, B. Ku, C. J. Kang and C. Choi, *Nanoscale*, 2020, **12**, 14120-14134.
141. A. Ali, H. Abbas, M. Hussain, S. H. A. Jaffery, S. Hussain, C. Choi and J. Jung, *Nano Research*, 2021, **15**, 2263-2277.
142. Q. Duan, Z. Jing, X. Zou, Y. Wang, K. Yang, T. Zhang, S. Wu, R. Huang and Y. Yang, *Nature Communications*, 2020, **11**, 3399.
143. H. Abbas, J. Li and D. S. Ang, *Micromachines*, 2022, **13**, 725.
144. P. Chen, X. Zhang, Z. Wu, Y. Wang, J. Zhu, Y. Hao, G. Feng, Y. Sun, T. Shi, M. Wang and Q. Liu, *IEEE Transactions on Electron Devices*, 2022, **69**, 2391-2397.
145. D. W. Kim, D. S. Woo, H. J. Kim, S. M. Jin, S. M. Jung, D. E. Kim, J. J. Kim, T. H. Shim and J. G. Park, *Advanced Electronic Materials*, 2022, **8**, 2101356.
146. J. Park, H. Ryu and S. Kim, *Scientific Reports*, 2021, **11**, 16601.
147. S. Choi, S. H. Tan, Z. Li, Y. Kim, C. Choi, P. Y. Chen, H. Yeon, S. Yu and J. Kim, *Nature Materials*, 2018, **17**, 335-340.
148. J. Wang, G. Cao, K. Sun, J. Lan, Y. Pei, J. Chen and X. Yan, *Nanoscale*, 2022, **14**, 1318-1326.
149. S. Park, A. Sheri, J. Kim, J. Noh, J. Jang, M. Jeon, B. Lee, B. R. Lee, B. H. Lee and H. Hwang, 2013 IEEE International Electron Devices Meeting, Washington, DC, USA, 2013.
150. J.-W. Jang, S. Park, Y.-H. Jeong and H. Hwang, 2014 IEEE International Symposium on Circuits and Systems (ISCAS), Melbourne, VIC, Australia, 2014.
151. A. M. Sheri, H. Hwang, M. Jeon and B.-g. Lee, *IEEE Transactions on Industrial Electronics*, 2014, **61**, 2933-2941.
152. J.-W. Jang, S. Park, G. W. Burr, H. Hwang and Y.-H. Jeong, *IEEE Electron Device Letters*, 2015, **36**, 457-459.
153. K. Moon, E. Cha, J. Park, S. Gi, M. Chu, K. Baek, B. Lee, S. Oh and H. Hwang, 2015 IEEE International Electron Devices Meeting (IEDM), Washington, DC, USA, 2015.
154. S. Park, M. Chu, J. Kim, J. Noh, M. Jeon, B. Hun Lee, H. Hwang, B. Lee and B. G. Lee, *Scientific Reports*, 2015, **5**, 10123.
155. A. Fumarola, Y. Leblebici, P. Narayanan, R. M. Shelby, L. L. Sanchez, G. W. Burr, K. Moon, J. Jang, H. Hwang and S. Sidler, 2019 19th Non-Volatile Memory Technology Symposium (NVMTS), Durham, NC, USA, 2019.
156. S. Yoo, Y. Wu, Y. Park and W. D. Lu, *Advanced Electronic Materials*, 2022, **0**, 2101025.
157. Q. Luo, X. Zhang, Y. Hu, T. Gong, X. Xu, P. Yuan, H. Ma, D. Dong, H. Lv, S. Long, Q. Liu and M. Liu, *IEEE Electron Device Letters*, 2018, **39**, 664-667.
158. K. M. Kim, J. Zhang, C. Graves, J. J. Yang, B. J. Choi, C. S. Hwang, Z. Li and R. S. Williams, *Nano Letters*, 2016, **16**, 6724-6732.
159. J. H. Yoon, S. J. Song, I.-H. Yoo, J. Y. Seok, K. J. Yoon, D. E. Kwon, T. H. Park and C. S. Hwang, *Advanced Functional Materials*, 2014, **24**, 5086-5095.
160. C. W. Hsu, I. T. Wang, C. L. Lo, M. C. Chiang, W. Y. Jang, C. H. Lin and T. H. Hou, 2013 Symposium on VLSI Technology, Kyoto, Japan, 2013.
161. A. Redaelli, A. Pirovano, A. Benvenuti and A. L. Lacaita, *Journal of Applied Physics*, 2008, **103**, 111101.
162. S. Meister, S. Kim, J. J. Cha, H.-S. P. Wong and Y. Cui, *ACS Nano*, 2011, **5**, 2742-2748.
163. D. Kuzum, R. G. Jeyasingh, B. Lee and H. S. Wong, *Nano Letters*, 2012, **12**, 2179-2186.
164. D. Kuzum, R. G. D. Jeyasingh, S. Yu and H. S. P. Wong, *IEEE Transactions on Electron Devices*, 2012, **59**, 3489-3494.
165. Y. Zhong, Y. Li, L. Xu and X. Miao, *physica status solidi (RRL) - Rapid Research Letters*, 2015, **9**, 414-419.
166. M. Suri, O. Bichler, D. Querlioz, O. Cueto, L. Perniola, V. Sousa, D. Vuillaume, C. Gamrat and B. Desalvo, 2011 International Electron Devices Meeting, Washington, DC, USA, 2011.
167. M. Suri, O. Bichler, Q. Hubert, L. Perniola, V. Sousa, C. Jahan, D. Vuillaume, C. Gamrat and B. Desalvo, 2012 4th IEEE International Memory Workshop, Milan, Italy, 2012.
168. O. Bichler, M. Suri, D. Querlioz, D. Vuillaume, B. DeSalvo and C. Gamrat, *IEEE Transactions on Electron Devices*, 2012, **59**, 2206-2214.
169. B. L. Jackson, B. Rajendran, G. S. Corrado, M. Breitwisch, G. W. Burr, R. Cheek, K. Gopalakrishnan, S. Raoux, C. T. Rettner, A. Padilla, A. G. Schrott, R. S. Shenoy, B. N. Kurdi, C. H. Lam and D. S. Modha, *ACM Journal on Emerging Technologies in Computing Systems*, 2013, **9**, 1-20.
170. C. D. Wright, P. Hosseini and J. A. V. Diosdado, *Advanced Functional Materials*, 2012, **23**, 2248-2254.
171. I. Boybat, M. Le Gallo, S. R. Nandakumar, T. Moraitis, T. Parnell, T. Tuma, B. Rajendran, Y. Leblebici, A. Sebastian and E. Eleftheriou, *Nature Communications*, 2018, **9**, 2514.
172. A. Sebastian, T. Tuma, N. Papandreou, M. Le Gallo, L. Kull, T. Parnell and E. Eleftheriou, *Nature Communications*, 2017, **8**, 1115.
173. T. Tuma, A. Pantazi, M. Le Gallo, A. Sebastian and E. Eleftheriou, *Nature Nanotechnology*, 2016, **11**, 693-699.

This journal is © The Royal Society of Chemistry 20xx

Please do not adjust margins

Please do not adjust margins

174. S. R. Nandakumar, M. Le Gallo, I. Boybat, B. Rajendran, A. Sebastian and E. Eleftheriou, *Journal of Applied Physics*, 2018, **124**, 152135.
175. J. Grollier, D. Querlioz, K. Y. Camsari, K. Everschor-Sitte, S. Fukami and M. D. Stiles, *Nature Electronics*, 2020, **3**, 360-370.
176. L. Berger, *Physical Review B: Condensed Matter and Materials*, 1996, **54**, 9353-9358.
177. J. C. Slonczewski, *Journal of Magnetism and Magnetic Materials*, 1996, **159**, L1-L7.
178. M. Gajek, J. J. Nowak, J. Z. Sun, P. L. Trouilloud, E. J. O'Sullivan, D. W. Abraham, M. C. Gaidis, G. Hu, S. Brown, Y. Zhu, R. P. Robertazzi, W. J. Gallagher and D. C. Worledge, *Applied Physics Letters*, 2012, **100**, 132408.
179. Q. Shao, Z. Wang and J. J. Yang, *Nature Electronics*, 2022, **5**, 67-68.
180. A. F. Vincent, J. Larroque, W. S. Zhao, N. B. Romdhane, O. Bichler, C. Gamrat, J.-O. Klein, S. Galdin-Retailleau and D. Querlioz, 2014 IEEE International Symposium on Circuits and Systems (ISCAS), Melbourne, VIC, Australia, 2014.
181. A. F. Vincent, J. Larroque, N. Locatelli, N. Ben Romdhane, O. Bichler, C. Gamrat, W. S. Zhao, J. O. Klein, S. Galdin-Retailleau and D. Querlioz, *IEEE Transactions on Biomedical Circuits and Systems*, 2015, **9**, 166-174.
182. Z. Diao, Z. Li, S. Wang, Y. Ding, A. Panchula, E. Chen, L.-C. Wang and Y. Huai, *Journal of Physics: Condensed Matter*, 2007, **19**, 165209.
183. Y. Lakys, W. S. Zhao, T. Devolder, Y. Zhang, J. Klein, D. Ravelosona and C. Chappert, *IEEE Transactions on Magnetics*, 2012, **48**, 2403-2406.
184. Y. Zhang, W. Zhao, G. Prenat, T. Devolder, J. Klein, C. Chappert, B. Dieny and D. Ravelosona, *IEEE Transactions on Magnetics*, 2013, **49**, 4375-4378.
185. T. Devolder, J. Hayakawa, K. Ito, H. Takahashi, S. Ikeda, P. Crozat, N. Zerounian, J.-V. Kim, C. Chappert and H. Ohno, *Physical Review Letters*, 2008, **100**, 057206.
186. D. Bedau, H. Liu, J. Z. Sun, J. A. Katine, E. E. Fullerton, S. Mangin and A. D. Kent, *Applied Physics Letters*, 2010, **97**, 262502.
187. J. Zhou, T. Zhao, X. Shu, L. Liu, W. Lin, S. Chen, S. Shi, X. Yan, X. Liu and J. Chen, *Advanced Materials*, 2021, **33**, 2103672.
188. S. Yang, J. Shin, T. Kim, K.-W. Moon, J. Kim, G. Jang, D. S. Hyeon, J. Yang, C. Hwang, Y. Jeong and J. P. Hong, *NPG Asia Materials*, 2021, **13**, 11.
189. S.-W. Chung, T. Kishi, J. W. Park, M. Yoshikawa, K. S. Park, T. Nagase, K. Sunouchi, H. Kanaya, G. C. Kim, K. Noma, M. S. Lee, A. Yamamoto, K. M. Rho, K. Tsuchida, S. J. Chung, J. Y. Yi, H. S. Kim, Y. S. Chun, H. Oyamatsu and S. J. Hong, 2016 IEEE International Electron Devices Meeting (IEDM), San Francisco, CA, USA, 2016.
190. M. Mansueto, A. Chavent, S. Auffret, I. Joumard, L. Vila, R. C. Sousa, L. D. Buda-Prejbeanu, I. L. Prejbeanu and B. Dieny, *Nanoscale*, 2021, **13**, 11488-11496.
191. Z. Yang, K. He, Z. Zhang, Y. Lu, Z. Li, Y. Wang, Z. Wang and W. Zhao, *IEEE Transactions on Electron Devices*, 2022, **69**, 1698-1705.
192. J. Valasek, *Physical Review*, 1921, **17**, 475-481.
193. S. H. Noh, W. Choi, M. S. Oh, D. K. Hwang, K. Lee, S. Im, S. Jang and E. Kim, *Applied Physics Letters*, 2007, **90**, 253504.
194. Y. Kato, Y. Kaneko, H. Tanaka and Y. Shimada, *Japanese Journal of Applied Physics*, 2008, **47**, 2719-2724.
195. X. Yin, X. Chen, M. Niemier and X. S. Hu, *IEEE Transactions on Very Large Scale Integration (VLSI) Systems*, 2019, **27**, 159-172.
196. H. Kohlstedt, N. A. Pertsev, J. Rodríguez Contreras and R. Waser, *Physical Review B*, 2005, **72**, 125341.
197. M. Y. Zhuravlev, R. F. Sabirianov, S. S. Jaswal and E. Y. Tsymbal, *Physical Review Letters*, 2005, **94**, 246802.
198. A. Chanthbouala, V. Garcia, R. O. Cherifi, K. Bouzehouane, S. Fusil, X. Moya, S. Xavier, H. Yamada, C. Deranlot, N. D. Mathur, M. Bibes, A. Barthélémy and J. Grollier, *Nature Materials*, 2012, **11**, 860-864.
199. Z. Wang, W. Zhao, W. Kang, Y. Zhang, J.-O. Klein and C. Chappert, 2014 International Joint Conference on Neural Networks (IJCNN), Beijing, China, 2014.
200. Z. Wang, W. Zhao, W. Kang, Y. Zhang, J.-O. Klein, D. Ravelosona and C. Chappert, *Applied Physics Letters*, 2014, **104**, 053505.
201. C. Ma, Z. Luo, W. Huang, L. Zhao, Q. Chen, Y. Lin, X. Liu, Z. Chen, C. Liu, H. Sun, X. Jin, Y. Yin and X. Li, *Nature Communications*, 2020, **11**, 1439.
202. X. Long, H. Tan, F. Sánchez, I. Fina and J. Fontcuberta, *Nature Communications*, 2021, **12**, 382.
203. H. Sun, Z. Luo, L. Zhao, C. Liu, C. Ma, Y. Lin, G. Gao, Z. Chen, Z. Bao, X. Jin, Y. Yin and X. Li, *ACS Applied Electronic Materials*, 2020, **2**, 1081-1089.
204. Z. Zhao, A. Abdelsamie, R. Guo, S. Shi, J. Zhao, W. Lin, K. Sun, J. Wang, J. Wang, X. Yan and J. Chen, *Nano Research*, 2021, **15**, 2682–2688.
205. L. Chen, T.-Y. Wang, Y.-W. Dai, M.-Y. Cha, H. Zhu, Q.-Q. Sun, S.-J. Ding, P. Zhou, L. Chua and D. W. Zhang, *Nanoscale*, 2018, **10**, 15826-15833.
206. H. Ryu, H. Wu, F. Rao and W. Zhu, *Scientific Reports*, 2019, **9**, 20383.
207. L. Bégon‐Lours, M. Halter, F. M. Puglisi, L. Benatti, D. F. Falcone, Y. Popoff, D. Dávila Pineda, M. Sousa and B. J. Offrein, *Advanced Electronic Materials*, 2022, **8**, 2101395.
208. A. Sunbul, T. Ali, K. Mertens, R. Revello, D. Lehninger, F. Muller, M. Lederer, K. Kuhnel, M. Rudolph, S. Oehler, R. Hoffmann, K. Zimmermann, K. Biedermann, P. Schramm, M. Czernohorsky, K. Seidel, T. Kampfe and L. M. Eng, *IEEE Transactions on Electron Devices*, 2022, **69**, 808-815.
209. T. Mikolajick, M. H. Park, L. Begon‐Lours and S. Slesazeck, *Advanced Materials*, 2023, DOI: 10.1002/adma.202206042, 2206042.
210. K.-U. Demasius, A. Kirschen and S. Parkin, *Nature Electronics*, 2021, **4**, 748–756.
211. J. I. Wadiche and C. E. Jahr, *Neuron*, 2001, **32**, 301-313.
212. M. Rao, H. Tang, J. Wu, W. Song, M. Zhang, W. Yin, Y. Zhuo, F. Kiani, B. Chen, X. Jiang, H. Liu, H.-Y. Chen, R. Midya, F. Ye, H. Jiang, Z. Wang, M. Wu, M. Hu, H. Wang, Q. Xia, N. Ge, J. Li and J. J. Yang, *Nature*, 2023, **615**, 823-829.
213. W. Choi, M. Kwak, S. Heo, K. Lee, S. Lee and H. Hwang, 2021 IEEE International Electron Devices Meeting (IEDM), San Francisco, CA, USA, 2021.
214. Y. Fu, Y. Zhou, X. Huang, B. Gao, Y. He, Y. Li, Y. Chai and X. Miao, 2021 IEEE International Electron Devices Meeting (IEDM), San Francisco, CA, USA, 2021.
215. T. Chang, S.-H. Jo, K.-H. Kim, P. Sheridan, S. Gaba and W. Lu, *Applied Physics A*, 2011, **102**, 857-863.
216. H. Shima, M. Takahashi, Y. Naitoh and H. Akinaga, 2018 IEEE 2nd Electron Devices Technology and Manufacturing Conference (EDTM), Kobe, Japan, 2018.
217. C. Mahata, C. Lee, Y. An, M.-H. Kim, S. Bang, C. S. Kim, J.-H. Ryu, S. Kim, H. Kim and B.-G. Park, *Journal of Alloys and Compounds*, 2020, **826**, 154434.
218. I. Oh, J. Pyo and S. Kim, *Nanomaterials*, 2022, **12**, 2185.

Please do not adjust margins

Please do not adjust margins

219. Y. Zhang, P. Huang, L. Cai, Y. Feng, L. Liu, X. Liu and J. Kang, *IEEE Electron Device Letters*, 2022, **43**, 1203-1206.
220. M. Kumar, S. S. Bezugam, S. Khan and M. Suri, *IEEE Transactions on Electron Devices*, 2021, **68**, 3346-3352.
221. E. Covi, S. Brivio, M. Fanciulli and S. Spiga, *Microelectronic Engineering*, 2015, **147**, 41-44.
222. Y. Li, Y. Zhong, J. Zhang, L. Xu, Q. Wang, H. Sun, H. Tong, X. Cheng and X. Miao, *Scientific Reports*, 2015, **4**, 4906.
223. Y. Shi, X. Liang, B. Yuan, V. Chen, H. Li, F. Hui, Z. Yu, F. Yuan, E. Pop, H.-S. P. Wong and M. Lanza, *Nature Electronics*, 2018, **1**, 458-465.
224. B. Ku, Y. Abbas, A. S. Sokolov and C. Choi, *Journal of Alloys and Compounds*, 2018, **735**, 1181-1188.
225. A. Senapati, S. Ginnaram, M. Dutta and S. Maikap, 2020 International Symposium on VLSI Technology, Systems and Applications (VLSI-TSA), Hsinchu, Taiwan, 2020.
226. C.-L. Hsu, A. Saleem, A. Singh, D. Kumar and T.-Y. Tseng, *IEEE Transactions on Electron Devices*, 2021, **68**, 5578-5584.
227. M. Zhao, S. Wang, D. Li, R. Wang, F. Li, M. Wu, K. Liang, H. Ren, X. Zheng, C. Guo, X. Ma, B. Zhu, H. Wang and Y. Hao, *Advanced Electronic Materials*, 2022, DOI: 10.1002/aelm.202101139, 2101139.
228. A. Ali, H. Abbas, M. Hussain, S. H. A. Jaffery, S. Hussain, C. Choi and J. Jung, *Applied Materials Today*, 2022, **29**, 101554.
229. L. Gao, T. Wang, P.-Y. Chen, S. Vrudhula, J.-s. Seo, Y. Cao, T.-H. Hou and S. Yu, *Nanotechnology*, 2015, **26**, 455204.
230. L. Tu, S. Yuan, J. Xu, K. Yang, P. Wang, X. Cui, X. Zhang, J. Wang, Y.-Q. Zhan and L.-R. Zheng, *RSC Advances*, 2018, **8**, 26549-26553.
231. S. Majumdar, H. Tan, Q. H. Qin and S. Van Dijken, *Advanced Electronic Materials*, 2019, **5**, 1800795.
232. S. Choi, G. S. Kim, J. Yang, H. Cho, C. Y. Kang and G. Wang, *Advanced Materials*, 2022, **34**, 2104598.
233. P. Bousoulas, C. Tsioustas, J. Hadfield, V. Aslanidis, S. Limberopoulos and D. Tsoukalas, *IEEE Transactions on Electron Devices*, 2022, **69**, 2360-2367.
234. T. Kim, S. H. Kim, J. H. Park, J. Park, E. Park, S. G. Kim and H. Y. Yu, *Advanced Electronic Materials*, 2021, **7**, 2000410.
235. Y.-F. Lu, Y. Li, H. Li, T.-Q. Wan, X. Huang, Y.-H. He and X. Miao, *IEEE Electron Device Letters*, 2020, **41**, 1245-1248.
236. S. Hao, X. Ji, S. Zhong, K. Y. Pang, K. G. Lim, T. C. Chong and R. Zhao, *Advanced Electronic Materials*, 2020, **6**, 1901335.
237. D. Dev, A. Krishnaprasad, M. S. Shawkat, Z. He, S. Das, D. Fan, H.-S. Chung, Y. Jung and T. Roy, *IEEE Electron Device Letters*, 2020, **41**, 936-939.
238. H. Kalita, A. Krishnaprasad, N. Choudhary, S. Das, D. Dev, Y. Ding, L. Tetard, H.-S. Chung, Y. Jung and T. Roy, *Scientific Reports*, 2019, **9**, 53.
239. X. Ji, C. Wang, K. G. Lim, C. C. Tan, T. C. Chong and R. Zhao, *ACS Applied Materials & Interfaces*, 2019, **11**, 20965-20972.
240. Y. Chen, Y. Wang, Y. Luo, X. Liu, Y. Wang, F. Gao, J. Xu, E. Hu, S. Samanta, X. Wan, X. Lian, J. Xiao and Y. Tong, *IEEE Electron Device Letters*, 2019, **40**, 1686-1689.
241. Y. Zhang, W. He, Y. Wu, K. Huang, Y. Shen, J. Su, Y. Wang, Z. Zhang, X. Ji, G. Li, H. Zhang, S. Song, H. Li, L. Sun, R. Zhao and L. Shi, *Small*, 2018, **14**, 1802188.
242. S. Lashkare, S. Chouhan, T. Chavan, A. Bhat, P. Kumbhare and U. Ganguly, *IEEE Electron Device Letters*, 2018, **39**, 484-487.
243. M. Jerry, A. Parihar, B. Grisafe, A. Raychowdhury and S. Datta, 2017 Symposium on VLSI Technology, Kyoto, Japan, 2017.
244. Y. Shi, L. Nguyen, S. Oh, X. Liu, F. Koushan, J. R. Jameson and D. Kuzum, *Nature Communications*, 2018, **9**, 5312.
245. D. V. Christensen, R. Dittmann, B. Linares-Barranco, A. Sebastian, M. Le Gallo, A. Redaelli, S. Slesazeck, T. Mikolajick, S. Spiga, S. Menzel, I. Valov, G. Milano, C. Ricciardi, S.-J. Liang, F. Miao, M. Lanza, T. J. Quill, S. T. Keene, A. Salleo, J. Grollier, D. Marković, A. Mizrahi, P. Yao, J. J. Yang, G. Indiveri, J. P. Strachan, S. Datta, E. Vianello, A. Valentian, J. Feldmann, X. Li, W. H. P. Pernice, H. Bhaskaran, S. Furber, E. Neftci, F. Scherr, W. Maass, S. Ramaswamy, J. Tapson, P. Panda, Y. Kim, G. Tanaka, S. Thorpe, C. Bartolozzi, T. A. Cleland, C. Posch, S. Liu, G. Panuccio, M. Mahmud, A. N. Mazumder, M. Hosseini, T. Mohsenin, E. Donati, S. Tolu, R. Galeazzi, M. E. Christensen, S. Holm, D. Ielmini and N. Pryds, *Neuromorphic Computing and Engineering*, 2022, **2**, 022501.
246. S. Ambrogio, P. Narayanan, H. Tsai, R. M. Shelby, I. Boybat, C. di Nolfo, S. Sidler, M. Giordano, M. Bodini, N. C. P. Farinha, B. Killeen, C. Cheng, Y. Jaoudi and G. W. Burr, *Nature*, 2018, **558**, 60-67.
247. D. Querlioz, O. Bichler and C. Gamrat, The 2011 International Joint Conference on Neural Networks, San Jose, CA, USA, 2011.
248. H. C. Woo, J. Kim, S. Lee, H. J. Kim and C. S. Hwang, *Advanced Electronic Materials*, 2022, **8**, 2200656.
249. M. Ismail, H. Abbas, A. Sokolov, C. Mahata, C. Choi and S. Kim, *Ceramics International*, 2021, **47**, 30764-30776.
250. W.-C. Chen, F. Huang, S. Qin, Z. Yu, Q. Lin, P. C. Mcintyre, S. S. Wong and H.-S. P. Wong, 2022 IEEE Symposium on VLSI Technology and Circuits (VLSI Technology and Circuits), Honolulu, HI, USA, 2022.
251. S. B. Eryilmaz, D. Kuzum, R. Jeyasingh, S. Kim, M. BrightSky, C. Lam and H.-S. P. Wong, *Frontiers in neuroscience*, 2014, **8**, 205.
252. C.-X. Xue, J.-M. Hung, H.-Y. Kao, Y.-H. Huang, S.-P. Huang, F.-C. Chang, P. Chen, T.-W. Liu, C.-J. Jhang, C.-I. Su, W.-S. Khwa, C.-C. Lo, R.-S. Liu, C.-C. Hsieh, K.-T. Tang, Y.-D. Chih, T.-Y. J. Chang and M.-F. Chang, 2021 IEEE International Solid- State Circuits Conference (ISSCC), San Francisco, CA, USA, 2021.
253. C.-X. Xue, W.-H. Chen, J.-S. Liu, J.-F. Li, W.-Y. Lin, W.-E. Lin, J.-H. Wang, W.-C. Wei, T.-W. Chang, T.-C. Chang, T.-Y. Huang, H.-Y. Kao, S.-Y. Wei, Y.-C. Chiu, C.-Y. Lee, C.-C. Lo, Y.-C. King, C.-J. Lin, R.-S. Liu, C.-C. Hsieh, K.-T. Tang and M.-F. Chang, 2019 IEEE International Solid- State Circuits Conference - (ISSCC), San Francisco, CA, USA, 2019.

This journal is © The Royal Society of Chemistry 20xx

Please do not adjust margins